The spreading of volatile liquid droplets on heated surfaces

D. M. Anderson[a] and S. H. Davis
Department of Engineering Sciences and Applied Mathematics, Northwestern University, Evanston, Illinois 60208

(Received 6 July 1994; accepted 11 October 1994)

A two-dimensional volatile liquid droplet on a uniformly heated horizontal surface is considered. Lubrication theory is used to describe the effects of capillarity, thermocapillarity, vapor recoil, viscous spreading, contact-angle hysteresis, and mass loss on the behavior of the droplet. A new contact-line condition based on mass balance is formulated and used, which represents a leading-order superposition of spreading and evaporative effects. Evolution equations for steady and unsteady droplet profiles are found and solved for small and large capillary numbers. In the steady evaporation case, the steady contact angle, which represents a balance between viscous spreading effects and evaporative effects, is larger than the advancing contact angle. This new angle is also observed over much of the droplet lifetime during unsteady evaporation. Further, in the unsteady case, effects which tend to decrease (increase) the contact angle promote (delay) evaporation. In the "large" capillary number limit, matched asymptotics are used to describe the droplet profile; away from the contact line the shape is determined by initial conditions and bulk mass loss, while near the contact-line surface curvature and slip are important. © *1995 American Institute of Physics.*

I. INTRODUCTION

Many processing systems involve trijunctions where phase transformations occur. Czochralski, and other meniscus-defined, crystal growth configurations are examples. They also appear in enclosed configurations such as directional solidification. An important instance of trijunction behavior involves a contact line across which evaporation/condensation occurs. For example, the behavior of the meniscus is critical in the heat transfer properties of a heat pipe, where a liquid layer is used to remove heat from a hot surface.

Theoretical and experimental work related to evaporation at contact lines has focused on microscopic details of the region. Renk and Wayner studied experimentally[1] and analytically[2] a steady evaporating meniscus in which capillary-induced flow toward the meniscus balanced the liquid lost due to evaporation. They found that the evaporating-meniscus profile was a function of the evaporative heat flux. Moosman and Homsy[3] followed with a more detailed analysis of the same configuration in which they included the effects of the meniscus extending to an adsorbed liquid layer. They reported an increase in the apparent contact angle when evaporation is present. Sujanani and Wayner[4] studied experimentally a similar configuration and observed an increase in the contact angle on microscopic scales when evaporation is present. Ripple[5] analyzed the motion of a meniscus on a heated surface on microscopic scales, where the contact-line region extends to a monolayer away from the bulk fluid. He described the effects of evaporation, thermocapillarity, and intermolecular forces on the meniscus. He found that the microscopic contact angle could be calculated and that it increased with increasing evaporation rate. Wayner[6] analyzed the motion of a meniscus due to an evaporation/condensation process wherein liquid evaporates from the thicker portion of the layer and condenses on a microscopic film ahead of the meniscus. He correlated an increase in the macroscopic contact angle with contact-line motion due to this evaporation/condensation process.

Although the modeling of evaporation on microscopic scales has led to information on macroscopic contact angles, the precise description is still unclear. The aim of the present work is to describe the evaporation process macroscopically.

There have been macroscopic descriptions of nonvolatile liquid droplets. Ehrhard and Davis[7] analyzed the behavior of a nonisothermal liquid droplet on a uniformly heated horizontal surface and described the effects of capillarity, thermocapillarity, gravity, and viscous spreading on the dynamics of the droplet. They found that thermocapillarity retards (promotes) spreading when the substrate is heated (cooled). Ehrhard[8] performed experiments on both isothermal and nonisothermal droplets and found good agreement with the theoretical predictions of Ehrhard and Davis.[7]

In the present work, we consider a two-dimensional volatile liquid droplet on a uniformly heated horizontal surface. We use lubrication theory to describe the effects of capillarity, thermocapillarity, viscous spreading, and mass loss on the behavior of the droplet. The evaporation model and the small-slope analysis is analogous to that of Burelbach, Bankoff, and Davis[9] for continuous films; however, in the present case there is a contact-line region which requires additional attention. The current work extends that of Ehrhard and Davis[7] to the competition between the effects of evaporation and the tendency of the drop to spread or recede. In Sec. II we discuss the one-sided model for the evaporation of a two-dimensional volatile liquid droplet on a uniformly heated plate. In Sec. III we formulate a new contact-line condition, based on a mass balance at the contact line, which represents a first step in understanding how viscous spreading and evaporation affect contact-line dynamics. In Sec. IV we obtain an evolution equation for the two-dimensional

[a]Present address: Department of Applied Mathematics and Theoretical Physics, University of Cambridge, Silver Street, Cambridge, CB3 9EW, United Kingdom.

 1070-6631/95/7(2)/248/18/$6.00

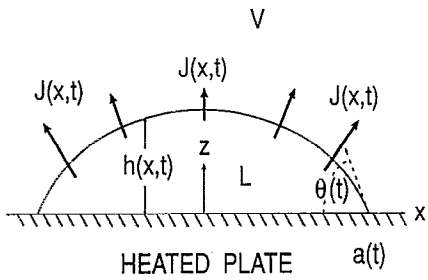

FIG. 1. The two-dimensional evaporating droplet. The contact-line location is given by $x=a(t)$, the contact angle by $\theta(t)$, and the liquid–vapor interface location by $z=h(x,t)$. The bottom plate, at $z=0$, is uniformly heated and there is a resulting evaporative mass flux, $J(x,t)$.

droplet profile based on a lubrication approximation. In Sec. V we consider a steady droplet profile obtained by balancing evaporative mass loss with an influx of mass through a source in the base. This leads to a steady contact angle, representing a balance of viscous spreading effects and evaporative effects, which is *different* from the steady contact angle achieved when no evaporation is present. In Sec. VI we consider the unsteady droplet dynamics in several limits and discuss results for water and ethanol drops. Here we find that several cases lead to a constant contact angle, which is the same steady contact angle as described above, over much of the droplet lifetime. Finally, in Sec. VII we summarize the results.

II. FORMULATION: ONE-SIDED MODEL

We consider a two-dimensional droplet of a volatile liquid on a uniformly heated horizontal surface as shown in Fig. 1. The liquid–vapor interface is given by $z=h(x,t)$, with contact lines $x=\pm a(t)$, and contact angle $\theta(t)$. There is an evaporative mass flux, $J(x,t)$, through the liquid–vapor interface, to be determined. In general the dynamics of the liquid and vapor phases are coupled. However, we shall adapt the one-sided model of evaporation by Burelbach, Bankoff, and Davis[9] given for a *continuous* film, which effectively decouples the dynamics of the liquid from the dynamics of the vapor. The basis for this model is the assumption that the density, viscosity, and thermal conductivity in the vapor phase are negligible compared with that in the liquid phase. The exception to this is that the vapor density is *retained* when multiplied by the vapor velocity, which may be large. This is analogous to a Boussinesq approximation in buoyancy-driven convection where density variations are neglected except when multiplied by gravity. This one-sided model allows for the determination of the liquid–vapor interface position without the necessity of computing the thermal and flow fields in the vapor phase. We shall only highlight the details of this model which are modified in the present analysis and those which are important in the understanding of the physical mechanisms to be studied.

The flow is assumed to be incompressible, and governed by the Navier–Stokes equations. The temperature is governed by the thermal diffusion equation. In order to take into account the presence of the contact line, the one-sided model here is modified by the inclusion of slip, measured by a constant slip coefficient, β^* (e.g., Dussan V.,[10] Davis,[11] and Ehrhard and Davis[7]). We shall neglect the effects of van der Waals attractions and gravity. The boundary conditions on the liquid–vapor interface are the mass balance, energy balance, the normal- and shear-stress balances, and a constitutive law relating temperature and mass flux.

We assume that the surface tension, σ, is linearly related to the local interface temperature, T_I, by

$$\sigma=\sigma_0-\gamma(T_I-T_S), \tag{1}$$

where σ_0 is the reference value of surface tension, γ is a positive constant, and T_S is the saturation temperature. This gives rise to thermocapillary effects through the balance of shear stress with surface tension gradients along the liquid–vapor interface. Surface tension variations in the normal-stress boundary condition are taken to be higher-order effects (small capillary number) and are not included in this analysis.

The normal-stress boundary condition represents a balance of the constant value of surface tension times curvature with a pressure jump across the interface plus an additional normal force associated with the vaporizing particles. This additional force appears in the normal-stress boundary condition as a product of mass flux times the jump in the normal velocities between the liquid and the vapor phases. Since mass is conserved at the evaporating interface, the slowly moving liquid particles are accelerated dramatically upon evaporation owing to the highly disparate densities between the vapor and the liquid. As a result of the vapor velocity being much larger than the liquid velocity, the additional normal force is, to leading order, just the product of the mass flux times the vapor velocity. This normal force can be thought of as an additional pressure acting down on the liquid–vapor interface. This normal force, or pressure, exerted on the liquid–vapor interface by these escaping particles is called vapor recoil (see also Palmer[12] and Burelbach, Bankoff, and Davis[9]).

The final boundary condition that we shall highlight here involves a linearized constitutive equation, which relates the mass flux, J, to the local interface temperature. Following Burelbach, Bankoff, and Davis[9] we take this to be

$$K^*J=T_I-T_S, \tag{2}$$

where the constant K^* measures the degree of nonequilibrium at the evaporating interface and is related to material properties. The derivation of this equation is based on kinetic theory (e.g., see Wayner[13] and Carey[14]). When $K^*\to 0$, corresponding to a highly volatile droplet, the interface temperature approaches the saturation temperature nonuniformly; there is a rapid relaxation of the temperature near the contact line. The case $K^*=0$ gives infinite heat flux at the contact line. The limit $K^*\to\infty$ corresponds to a nonvolatile droplet where there is zero mass flux, $J=0$.

III. CONTACT-LINE DYNAMICS

Since both the contact line and the liquid–vapor interface are free boundaries, additional information is needed in order to determine the contact-line position. Empirical studies (see Dussan V.[10]) on the spreading behavior of *nonvola-*

tile liquid droplets have led to the use of a constitutive relation between fluid velocity at the contact line, u_{CL}, and the contact angle given by

$$u_{CL}=\eta f(\theta), \tag{3a}$$

where $f(\theta)$ is an increasing function of θ given by

$$f(\theta)=\begin{cases}(\theta-\theta_A)^m & \text{for } \theta>\theta_A,\\ 0 & \text{for } \theta_R<\theta<\theta_A,\\ (\theta-\theta_R)^m & \text{for } \theta<\theta_R,\end{cases} \tag{3b}$$

where η and m are empirically determined constants (in general the value of η may differ for $\theta>\theta_A$ and for $\theta<\theta_R$; however, for simplicity, we take here a single value). Here θ_A is the advancing contact angle and θ_R is the receding contact angle. Contact-angle hysteresis is present when $\theta_A\neq\theta_R$. Then, when $\theta\in[\theta_R,\theta_A]$, the contact line is static. The value, $m=3$, for the mobility exponent is in agreement with experimental results by Schwartz and Tejada,[15] Hoffman,[16] and Ehrhard.[8]

When evaporation is present, the mass balance at the contact line is

$$\frac{da}{dt}=-\frac{J(a)}{\rho_L \sin\theta(t)}+u_{CL}. \tag{4}$$

This new condition shows that the speed of the contact line is *not* equal to the fluid velocity there; the difference being related to the mass loss. When there is no evaporation, $J=0$, this equation reduces to the nonvolatile result where the speed of the contact line is equal to the fluid velocity. This condition also shows that even when the fluid is at rest, $u_{CL}=0$, the contact line still can move as a result of mass loss.

Since the contact-line speed, da/dt, and the fluid velocity, u_{CL}, are distinct, previous data on u_{CL} vs θ do not apply here and there are no data known to the authors that represent u_{CL} when phase transformation is present. Thus, we must pose a constitutive relation that is plausible and reduces to known cases in special limits. We take this to be of the same form as in the nonvolatile case and write $u_{CL}=\eta f(\theta)$. We combine this with Eq. (4) to give

$$\frac{da}{dt}=-\frac{J(a)}{\rho_L \sin\theta(t)}+\eta f(\theta). \tag{5}$$

When evaporation is absent, Eq. (5) reduces to the nonvolatile case. The assumed form can be thought of as a leading-order superposition of the effects of (weak) mass loss and the effects of (weak) viscous spreading acting to determine the contact-line motion.

We can further understand the form (5) by writing θ as a function of da/dt and $J(a)$, viz.,

$$(\theta-\theta_M)^m=F\left(\frac{da}{dt},J(a)\right), \tag{6}$$

where θ_M represents either θ_A or θ_R depending on the sign of da/dt. If both $|da/dt|$ and $|J(a)|$ were small, then

$$(\theta-\theta_M)^m\sim\left(\frac{da}{dt}\right)F_{da/dt}(0,0)+J(a)F_{J(a)}(0,0) \tag{7}$$

and the partial derivatives can be identified as

$$F_{da/dt}(0,0)=\eta^{-1},\quad F_{J(a)}(0,0)=(\eta\rho_L \sin\theta_M)^{-1} \tag{8}$$

with η and m given by their nonevaporative values. Thus, we shall suppose that even when evaporation is present, $m=3$.

On a microscopic scale there have been suggestions that θ depends on the mass flux (e.g., Sujanani and Wayner[4] and Ripple[5]). Our suggestion is that this dependence of the contact angle on mass flux is also the case on the *micron* scale where effective slip occurs. We emphasize that, analogous to the nonvolatile case, the precise form of u_{CL} when evaporation is present must be determined empirically. An aim of the present work is to investigate a leading-order description of contact line behavior that can be tested experimentally.

IV. EVOLUTION EQUATION

We shall analyze this model using a lubrication approximation which is applicable for thin droplets. We adopt the following scales. The horizontal and vertical scales are the initial droplet radius, a_0 and height, $h_0=a_0\theta_0/2$, where θ_0 is the initial contact angle. The volume is scaled on $2a_0h_0$. The contact angle, θ, scales on the aspect ratio, $\epsilon\equiv h_0/a_0$. Standard lubrication scales are chosen for the velocities and pressure in which the pressure gradient balances the viscous term in the horizontal component of the Navier–Stokes equations. The temperature relative to the saturation temperature scales on the difference, $\Delta T=T_H-T_S$, between the imposed plate temperature and the saturation temperature. The mass flux scale is chosen from the energy balance on the interface to balance latent heat of vaporization with heat flux, and is given by $k\Delta T/h_0L$, where k is the thermal conductivity in the liquid and L is the latent heat. There is an evaporative time scale, $t_E=\rho_L h_0^2L/(k\Delta T)$ and also a viscous time scale $t_V=h_0^2/\nu$, where ρ_L is the density of the liquid, and ν is the kinematic viscosity of the liquid. We shall introduce a dimensionless time, τ, based on the slow viscous time scale, t_V/ϵ, which leads to quasisteady temperature and velocity fields.

We use a standard approach (e.g., see Greenspan,[17] Hocking,[18] Haley and Miksis,[19] and Ehrhard and Davis[7]) to derive an evolution equation for the droplet profile where the temperature, fluid velocities, and mass flux, can be written down in terms of h and its derivatives. Details of this calculation can be found in Anderson.[20] The evolution equation for the two-dimensional droplet profile, h, is

$$h_\tau+\frac{\tilde{E}}{K+h}+\frac{\partial}{\partial x}\left[\tilde{C}^{-1}h^2\left(\beta+\frac{1}{3}h\right)h_{xxx}\right.$$
$$\left.+\tilde{M}K\frac{h(\beta+\frac{1}{2}h)h_x}{(K+h)^2}+\frac{2\tilde{E}^2}{\tilde{\rho}}\frac{h^2(\beta+\frac{1}{3}h)h_x}{(K+h)^3}\right]=0. \tag{9}$$

The nondimensional parameters which arise here are

TABLE I. Nondimensional parameters for water and ethanol; $\bar{C}$=capillary number, $\bar{E}$=evaporation number, $\bar{M}$=Marangoni number, $\bar{\rho}$=density ratio, K=nonequilibrium parameter.

	Water	Ethanol
$\bar{C}^{-1}$ $(h_0/\text{cm})\epsilon^3$	6.8×10^{6}	1.0×10^{6}
$\bar{E}(1/\epsilon)$	1.0×10^{-2}	4.9×10^{-3}
$\bar{M}$ $(h_0/\text{cm})\epsilon$	2.1×10^{5}	4.5×10^{5}
$\bar{\rho}(1/\epsilon^3)$	6.3×10^{-4}	2.0×10^{-3}
K $(h_0/\text{cm})^{-1}$	8.3×10^{-6}	3.1×10^{-6}

$$\bar{E}=\frac{1}{\epsilon}\frac{k\Delta T}{\rho_L \nu L} \quad \text{(evaporation number)}, \tag{10a}$$

$$\beta=\frac{\beta^*}{h_0} \quad \text{(slip coefficient)}, \tag{10b}$$

$$\bar{\rho}=\frac{1}{\epsilon^3}\frac{\rho_V}{\rho_L} \quad \text{(density ratio)}, \tag{10c}$$

$$\bar{C}=\frac{1}{\epsilon^3}\frac{\rho_L \nu^2}{\sigma_0 h_0} \quad \text{(capillary number)}, \tag{10d}$$

$$\bar{M}=\epsilon\frac{\gamma\Delta T h_0}{\rho_L \nu^2} \quad \text{(Marangoni number)}, \tag{10e}$$

$$K=K^*\frac{k}{h_0 L} \quad \text{(nonequilibrium parameter)}. \tag{10f}$$

Note that the barred quantities have been scaled on the aspect ratio, similar to that done by Burelbach, Bankoff, and Davis,[9] and all the parameters listed in Eq. (10) are assumed to be $O(1)$ in the limit $\epsilon\to0$.

The first and second terms in Eq. (9) are the unsteady and mass-loss terms. Note that $\bar{E}$ is the ratio of the slow viscous time scale to the evaporative time scale and measures the strength of evaporation. The term multiplied by $\bar{C}^{-1}$ is the curvature term, and the last two terms correspond to thermocapillarity and vapor recoil, respectively. Table I shows typical values for the nondimensional parameters for water and ethanol (based on the physical constants listed in Burelbach, Bankoff, and Davis[9]).

Special cases of Eq. (9) have been derived by several authors. Greenspan[17] considered isothermal spreading of a two-dimensional or axisymmetric droplet and derived an evolution equation which included unsteady and capillary effects, using a slip coefficient $\beta\sim1/h$, and a contact angle linearly dependent on contact-line speed. Hocking[21] derived the analogous evolution equation, using a constant slip coefficient and a constant contact angle, describing the effects of capillarity and gravity on the motion of a two-dimensional droplet on an inclined plane and later[18] derived a similar equation for an axisymmetric drop for a horizontal surface. Burelbach, Bankoff, and Davis[9] derived an evolution equation including the effects shown in Eq. (9) plus an additional term due to van der Waals attractions. They considered continuous thin films without contact lines so that slip was not introduced ($\beta=0$). Ehrhard and Davis[7] derived an evolution equation which includes the nonevaporative thermal effects of Eq. (9) plus the effects of gravity. Their system, in the absence of gravity, can be recovered from ours by taking $\bar{E}=0$, $K=1/B$, where B is their Biot number, and then rescaling.

The other unknowns in the problem are related to h as follows. The mass flux is given by

$$J=\frac{1}{K+h} \tag{11}$$

and the temperature is given by

$$T=1-\frac{z}{K+h}. \tag{12}$$

Note that the mass flux varies in space and time through the droplet profile, h, and is strongest at the contact line where $h=0$. Here we see directly the effect of the nonequilibrium parameter, K, on the mass flux and temperature. The mass flux becomes increasingly strong as K gets smaller. As $K\to0$, the temperature of the interface approaches the saturation temperature everywhere except near the contact line, where it rapidly approaches the plate temperature. This corresponds to very large heat fluxes, and hence, very large mass fluxes, near the contact line. As $K\to\infty$, the temperature of the interface approaches the plate temperature. Here the heat flux and hence, mass flux, approach zero. The horizontal and vertical components of the fluid velocity, u and w, are likewise related to h. The specific forms can be found in Anderson.[20]

Equation (9) is subject to boundary and symmetry conditions,

$$h(a(\tau),\tau)=0, \tag{13a}$$

$$\frac{\partial h}{\partial x}(a(\tau),\tau)=-\Theta(\tau), \tag{13b}$$

$$\frac{\partial h}{\partial x}(0,\tau)=\frac{\partial^3 h}{\partial x^3}(0,\tau)=0; \tag{13c}$$

contact-line condition,

$$a_\tau(\tau)=-\frac{\bar{E}}{K\Theta(\tau)}+\bar{\eta}f(\Theta(\tau)); \tag{14}$$

and the global mass balance

$$\int_0^{a(\tau)}\left(h_\tau(x,\tau)+\frac{\bar{E}}{K+h(x,\tau)}\right)dx=0. \tag{15}$$

Here $\bar{\eta}=(\eta/\nu)\epsilon^m h_0$, and $f(\Theta)$ is given by Eq. (3b) with θ_A and θ_R replaced by Θ_A and Θ_R, where $(\theta,\theta_A,\theta_R)=\epsilon(\Theta,\Theta_A,\Theta_R)$. There are also initial conditions at the contact line, $a(0)=1$ and $\Theta(0)=2$, and on the droplet profile.

In contrast to past analyses, the volume of the droplet is not conserved; the rate of change of mass in the droplet is equal to the mass loss through the interface due to evaporation. Note that the contact-line condition and global mass-balance conditions reduce for $\bar{E}=0$ to those of viscous spreading and conservation of volume.

Table II shows representative values for the parameter appearing in Eqs. (9), (14), and (15) for water and ethanol systems. We have taken the value of K here to be larger than that shown in Table I for demonstration purposes. However,

TABLE II. Parameter values for different initial profiles for water and ethanol; $\bar{C}$=capillary number, $\bar{E}$=evaporation number, $\bar{M}$=Marangoni number, $\bar{\rho}$=density ratio, K=nonequilibrium parameter, β=slip coefficient, $\bar{\eta}$=characteristic spreading velocity, Θ_R=receding contact angle, Θ_A=advancing contact angle.

	$\epsilon=0.1$		$\epsilon=0.005$	
	Water	Ethanol	Water	Ethanol
$\bar{C}^{-1}$	6.8×10^{2}	1.0×10^{2}	1.9×10^{-2}	2.8×10^{-3}
$\bar{E}$	0.1	4.9×10^{-2}	2.0	0.98
K	2.0×10^{-3}	1.0×10^{-3}	1.0×10^{-2}	5.0×10^{-3}
$\bar{E}^2/\bar{\rho}$	1.6×10^{-2}	1.2×10^{-3}	7.9×10^{-4}	6.0×10^{-5}
$\bar{M}K$	0.17	0.14	8.7×10^{-3}	7.0×10^{-3}
β	0.01	0.01	0.04	0.04
$\bar{\eta}$	0.03	0.02	10^{-7}	10^{-7}
Θ_R	0.1	0.1	2.0	2.0
Θ_A	0.1	0.1	2.0	2.0

we can associate the value of K with the inverse of the Biot number used by Ehrhard and Davis[7] and therefore argue that a wider range of K, including larger ones, are relevant for these systems. Further, results in Secs. VI A and VI C show the significant quantitative changes in the results for small values of K. Two sets of values are shown; $\epsilon=0.1$ ($h_0=0.1$ cm and $a_0=1$ cm), and $\epsilon=0.005$ ($h_0=0.022\,36$ cm and $a_0=4.472$ cm). These values were chosen so that each case has the same initial volume. Only the initial configurations are different (thin, and thinner, respectively). Here, as an order of magnitude estimate for $\bar{\eta}$ we have taken $\eta\sim1$ cm/s [where $\bar{\eta}=(\eta/\nu)\epsilon^m h_0$] (Schwartz and Tejada[15]) and have also used $m=3$ for both water and ethanol. It should be noted that the exact values of η appropriate here are not known to the authors. These values will depend on specific properties of the substrate, and in general need to be determined experimentally.

The parameter values in Table II show that two general cases may be of interest; $\bar{C}^{-1}\gg\bar{E}$ and $\bar{C}^{-1}\ll\bar{E}$. Therefore, we shall consider two limits which simplify this system. First, we shall look at the small capillary number limit, $\bar{C}\to0$, where surface tension is dominant. Then, we shall look at the "large" capillary number limit, $\bar{C}^{-1}\to0$, where evaporation is the dominant mechanism determining the droplet profile. Our aim is to understand how the physical mechanisms involved interact in determining the dynamics of the droplet. After determining the general behavior, we shall show results for parameter values corresponding to water and ethanol drops.

V. STEADY SPREADING AND EVAPORATION

In order to focus on the effects of the mass loss on contact-angle dynamics, we shall define a steady, two-dimensional, evaporating droplet. Such a configuration, shown in Fig. 2, can be achieved by pumping liquid through a localized opening in the base of the droplet (away from the contact line) at a rate which exactly balances the mass loss through the interface due to evaporation. Although this configuration may be idealized, it does serve as a good illustration of certain principles and identifies an important balance at the contact line. One could also imagine the same type of

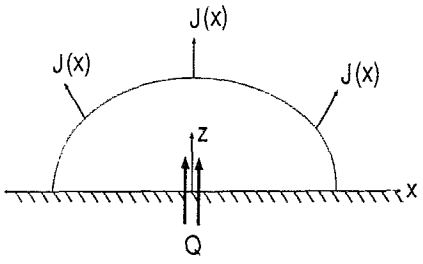

FIG. 2. The steady two-dimensional evaporating droplet with mass flux through the base. When the mass flux through the base balances the evaporative mass flux through the liquid–vapor interface, a steady droplet configuration can be achieved.

situation occurring at the leading edge of an evaporating liquid film on an incline where the amount mass being supplied by the flow down the incline is exactly matched by the amount lost due to evaporation, creating a steady configuration. Steady menisci at which phase transformation occurs are common in heat pipes, for example, and the configuration we treat here is fundamentally the same. The key results of this section will be largely independent of the particular steady configuration chosen to illustrate them.

The formulation of this problem is identical to the previous case with the exception that the boundary condition $w=0$ on $z=0$ is replaced by $w=W(x)$. With the assumption that $W(x)$ is sufficiently localized such that $W(a)=0$, we obtain the generalized evolutionary system similar to Eqs. (9), (14), and (15)

$$h_\tau+\frac{\bar{E}}{K+h}-W(x)+\frac{\partial}{\partial x}\left[\bar{C}^{-1}h^2\left(\beta+\frac{1}{3}h\right)h_{xxx}+\bar{M}K\,\frac{h(\beta+\frac{1}{2}h)h_x}{(K+h)^2}+\frac{2\bar{E}^2}{\bar{\rho}}\,\frac{h^2(\beta+\frac{1}{3}h)h_x}{(K+h)^3}\right]=0, \tag{16}$$

$$a_\tau(\tau)=-\frac{\bar{E}}{K\Theta(\tau)}+\bar{\eta}f(\Theta(\tau)), \tag{17}$$

and

$$\int_0^{a(\tau)}\left(h_\tau(x,\tau)+\frac{\bar{E}}{K+h(x,\tau)}\right)dx=\int_0^{a(\tau)}W(x)dx. \tag{18}$$

subject to the boundary conditions (13) and initial conditions.

Steady solutions satisfy the above system with all time derivatives set to zero. In this case, we immediately find that the contact-line condition (17) gives the steady value Θ_S of Θ, in which evaporative mass loss balances spreading. Since

$$\bar{\eta}f(\Theta_S)=\frac{\bar{E}}{K\Theta_S}>0, \tag{19}$$

$\Theta_S>\Theta_A$ *always*; evaporation gives an apparent angle *greater* than, possibly much greater than, Θ_A. Θ_S satisfies

$$\Theta_S(\Theta_S-\Theta_A)^m=\frac{\bar{E}}{K\bar{\eta}}. \tag{20}$$

This gives an explicit value for Θ_S on a macroscopic scale, which includes the effects due to phase transformation. Note

that this result is determined at the contact line and is not dependent on details of the profile away from the contact line. Therefore, this result holds for the steady evaporating droplet as well as for the leading edge of a steady evaporating liquid film, for example. We note here that Ripple[5] analyzed a microscopic evaporating contact line, which included intermolecular forces and an adsorbed liquid film, and predicted an increased *microscopic* contact angle with increased evaporation. Also, steady microscopic contact angles were achieved experimentally by Sujanani and Wayner[4] and were found to increase with increased evaporation. Information on *macroscopic* contact angles suggests that they also increase with evaporation (e.g., Moosman and Homsy[3] and Wayner[6]). Chung and Bankoff[22] found that their static rivulet and dry-patch models, which describe the breakdown of a volatile liquid film into rivulets, would be consistent with their experimental observations only if the contact angle were taken to be "large." Comparison of steady macroscopic contact angles found experimentally with the predictions of Eq. (20) may be the most direct way to test the range of validity of our contact-line condition.

For purposes of illustration we shall seek a solution of the evolution Eq. (16) with $\bar{C}=0$. This gives a parabolic profile

$$h(x)=\frac{\Theta_S}{2a_S}(a_S^2-x^2). \tag{21}$$

We substitute this into Eq. (18) and integrate to obtain

$$\frac{2\bar{E}a_S}{\Theta_S a_S^\dagger}\tanh^{-1}\left(\frac{a_S}{a_S^\dagger}\right)=\int_0^{a_S}W(x)dx\equiv Q, \tag{22}$$

where $a_S^\dagger=[a_S^2+(2a_SK/\Theta_S)]^{1/2}$, which determines the droplet radius, a_S, for a given inflow $W(x)$. Alternatively, for a given equilibrium volume, which fixes a_S, the necessary inflow is given from Eq. (22). It is important to note that while the drop profile and contact-line position are constant in time, there *is* fluid motion corresponding to the flow from the source to the droplet surface where it evaporates. This can be seen clearly from the original mass balance (4) which shows that u_{CL}, regardless of its form, must be positive for evaporation at a stationary contact line.

The effect of evaporation on the droplet profile can be seen if we compare a profile in this case, where $\Theta_S>\Theta_A$, with one in which no evaporation occurs, where $\Theta_S=\Theta_A$. Figure 3 shows two such profiles with the same initial conditions and equilibrium volume. Recall that h and x are scaled quantities and therefore the profiles do not appear to be "thin." Here $\Theta_A=0.1$, $\bar{E}=0.5$, $K=0.1$, $\bar{\eta}=0.1$, and $m=3$. The lower profile in Fig. 3 corresponds to the equilibrium configuration in the case of no evaporation. Here the drop has gone from its initial configuration to its equilibrium configuration solely due to viscous spreading. The steady profile shown is the taller one in Fig. 3 and has nonzero Q. Note that it has a slightly smaller radius than the initial radius of 1.0. These two profiles show that the presence of evaporation can have a dramatic effect on the equilibrium droplet profile, and in particular on the steady contact angle.

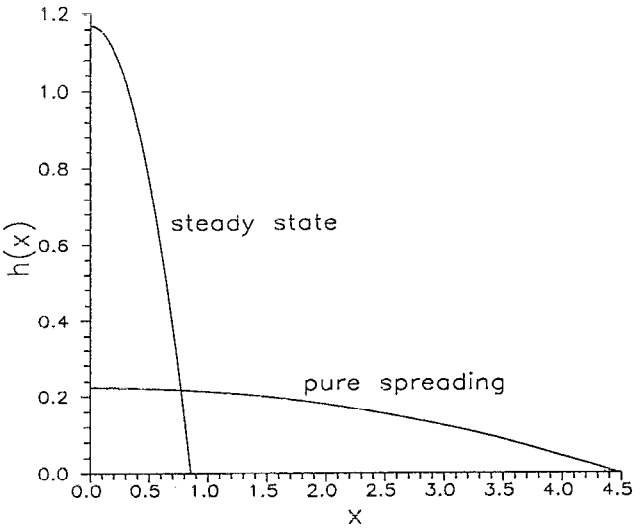

FIG. 3. Zero capillary number, steady spreading, and evaporation: Two droplet profiles with $\bar{C}=0$, $\Theta_A=\Theta_R=0.1$, $\bar{\eta}=0.1$, and $m=3$. The upper profile corresponds steady evaporation with $\bar{E}=0.5$ and $K=0.1$, and $Q=0.68$ while the lower profile corresponds to no evaporation: $\bar{E}=0$ and $Q=0$. Note that the shape is independent of β, $\bar{M}$, and $\bar{\rho}$ when $\bar{C}=0$. Both correspond to the same initial and final volumes and the same initial conditions, $a(0)=1$, $\Theta(0)=2$. Note that in the absence of evaporation the drop has spread to an equilibrium configuration with $\Theta_S=\Theta_A$ while with evaporation, the drop has receded to a smaller radius and $\Theta_S>\Theta_A$, as given by Eq. (20).

VI. UNSTEADY SPREADING AND EVAPORATION

We return to the two-dimensional droplet in the absence of injected fluid, $Q=0$. In the problems that follow, we shall be particularly interested in the implications of the contact-line condition (5) which we propose.

A. Zero capillary number

Consider equations (9), (14), and (15) for $\bar{C}=0$ with all other parameters $O(1)$. As discussed by Rosenblat and Davis,[23] this limit leads to an outer solution in time for the drop profile; the initial conditions on h are dropped while those at the contact line are enforced. We also note that the profiles calculated with $\bar{C}=0$ are independent of slip, thermocapillarity, and vapor recoil (i.e., independent of β, $\bar{M}$, and $\bar{\rho}$).

Note that if we integrate Eq. (9) in x from 0 to $a(\tau)$, taking into account symmetry, we obtain the global mass-balance equation (15). Therefore, solutions to the full time-dependent evolution equation automatically conserve mass globally. However, in the limit $\bar{C}\to 0$, we retain only the curvature term to leading order in Eq. (9) and hence must enforce the global mass-balance (15) separately in order to retain the effects of bulk evaporation. In this limit, the contact-line condition retains its time derivative and the contact-line dynamics is essential to the droplet motion.

The solution of the evolution equation (9) with $\bar{C}=0$ and satisfying boundary conditions (13) is given simply by

$$h(x,\tau)=\frac{\Theta}{2a}(a^2-x^2), \tag{23}$$

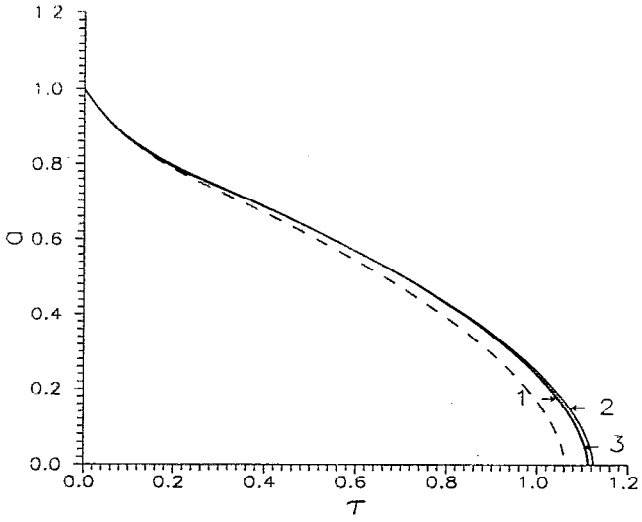

FIG. 4. Small capillary number, unsteady spreading, and evaporation: $a(\tau)$ vs τ showing the effects of the different mechanisms in the "strong" evaporation regime. Here $\bar{E}=0.5$, $K=0.1$, $\bar{\eta}=0.1$, $\Theta_R=\Theta_A=0.1$, and $m=3$. The dashed curve corresponds to $\bar{C}=0$ and is independent of the thermocapillary, vapor recoil, and unsteady and mass loss terms in the evolution equation, and the slip coefficient β. While the initial contact angle is significantly larger than the static advancing contact angle, the droplet radius decreases monotonically to zero. The solid curves correspond to $\bar{C}=0.1$ and have $\beta=0.5$. Solid curve #1 has $\bar{M}=0$ and $\bar{\rho}=\infty$ and isolates the effect of the unsteady and mass loss terms. Solid curve #2 has $\bar{M}=1.0$ and $\bar{\rho}=\infty$. Solid curve #3 (nearly overlapping but just outside curve #1) has $\bar{M}=0$ and $\bar{\rho}=10$. We see that in each of these cases, the droplet lifetime is increased from the $\bar{C}=0$ case.

where a and Θ are to be determined. This profile is the lubrication version of a constant curvature profile, where surface tension is dominant. The global mass balance (15) then gives

$$\frac{d}{d\tau}(\Theta a^2)=-6\bar{E}\,\frac{a}{\Theta a^{\dagger}}\tanh^{-1}\left(\frac{a}{a^{\dagger}}\right), \tag{24}$$

where $a^{\dagger}=[a^2+(2aK/\Theta)]^{1/2}$. This, coupled with Eq. (14) subject to initial conditions, gives an evolutionary system for a and Θ. Note that with $\bar{C}=0$ the droplet profile is independent of thermocapillarity and vapor recoil. We have solved this system numerically using a Runge–Kutta scheme (IMSL routine DIVPRK). The solution is quasisteady; the drop equilibrates instantaneously to the parabolic profile given in Eq. (23) and depends on time only through a and Θ, which evolve due to viscous spreading and bulk mass loss. In the analysis of this evolutionary system, we shall identify the effects of mass loss, viscous spreading, and contact-angle hysteresis.

In terms of the competition between viscous spreading and evaporation we find that there are two typical regimes. If we look at the contact-line condition (14) evaluated at $\tau=0$, we find that $a_\tau(0)$ can be either positive or negative. That is, although evaporation is present, $\bar{E}\neq 0$, and always results in the disappearance of the droplet, the droplet may still spread initially. Specifically, we find that if

$$-\frac{\bar{E}}{2K}+\bar{\eta}f(2)<0\ \ (>0)\rightarrow a_\tau(0)<0\ \ (>0). \tag{25}$$

We shall denote the first case, where $a_\tau(0)<0$, the "strong"-evaporation regime, and the second case, where $a_\tau(0)>0$, the "weak"-evaporation regime.

The following results correspond to $K=0.1$, $\bar{\eta}=0.1$, $\Theta_R=\Theta_A=0.1$, $m=3$; there is no contact-angle hysteresis. In the strong-evaporation case we take $\bar{E}=0.5$ while in the weak-evaporation case $\bar{E}=0.05$.

Solutions for the strong-evaporation regime are shown in Figs. 4 and 5, showing a vs τ and the corresponding value of Θ vs τ, respectively. In both figures, the dashed curve corresponds to the solution with $\bar{C}=0$, which has no corrections due to the unsteady and mass loss terms, thermocapillarity, or vapor recoil (solid curves in these figures correspond to $\bar{C}\neq 0$ and are discussed in the next section). Here we see that while the initial contact angle is significantly larger than the thermostatic advancing contact angle [$\Theta(0)=2$ while $\Theta_A=0.1$], evaporation is strong enough that the droplet never spreads. The droplet radius decreases monotonically to zero (see Fig. 4). The contact angle, Θ, increases initially to a relatively constant value, a contact-angle plateau, where it remains until the droplet has nearly disappeared (see Fig. 5). Note that this value is approximately 2.5 while the steady angle, Θ_S, given by Eq. (20) and representing a balance between viscous spreading and evaporative effects, is 2.73 for these parameter values. The results point out that it is possible for the system to maintain contact angles significantly larger than the static contact angle Θ_A, by balancing spreading and mass loss.

Solutions for the weak-evaporation regime are shown in Figs. 6 and 7. In both figures the dashed curve corresponds to the result for $\bar{C}=0$ (again, the solid curves have $\bar{C}\neq 0$ and

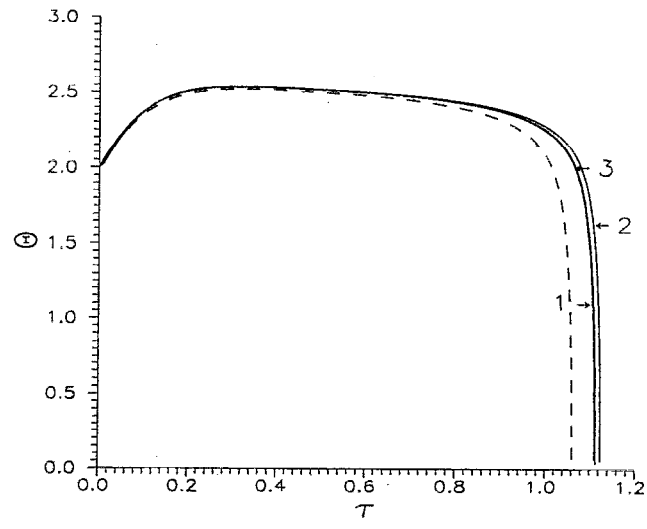

FIG. 5. Small capillary number, unsteady spreading, and evaporation: $\Theta(\tau)$ vs τ corresponding to Fig. 4. Here $\bar{E}=0.5$, $K=0.1$, $\bar{\eta}=0.1$, $\Theta_R=\Theta_A=0.1$, and $m=3$. The dashed curve corresponds to $\bar{C}=0$ and shows that Θ increases initially to a nearly constant value, where it remains until the droplet has nearly disappeared. This constant value is approximately Θ_S, the angle which is obtained by a balance of viscous spreading and evaporative effects at the contact line. Note that when $\bar{C}=0$ the droplet profile is independent of slip, Marangoni effects, and vapor recoil. The solid curves marked #1, #2, and #3 correspond to those in Fig. 4 having the same parameter values. In each case, the effect of these terms is to increase the contact angle from the $\bar{C}=0$ case and to slow evaporation.

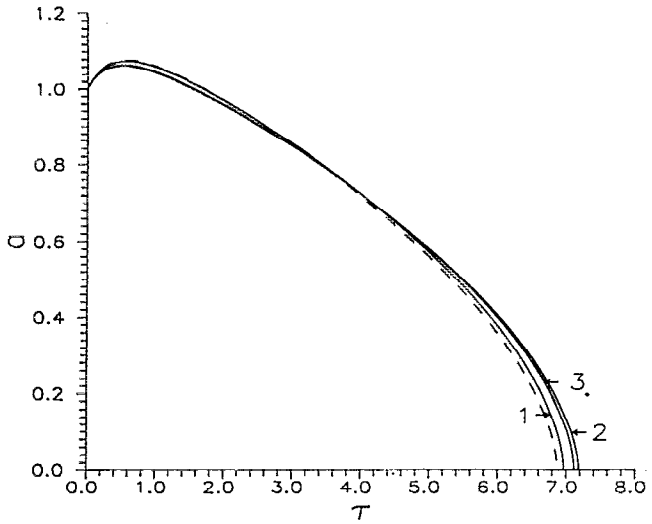

FIG. 6. Small capillary number, unsteady spreading, and evaporation: $a(\tau)$ vs τ showing the effect of the different mechanisms in the "weak" evaporation regime. Here $\bar{E}=0.05$, $K=0.1$, $\bar{\eta}=0.1$, $\Theta_R=\Theta_A=0.1$, and $m=3$. The dashed curve corresponds to $\bar{C}=0$. Now we see that the droplet spreads initially before eventually disappearing. The solid curves correspond to $\bar{C}=0.1$ and have $\beta=0.5$. Solid curve #1 has $\bar{M}=0$ and $\bar{\rho}=\infty$ and isolates the effect of the unsteady and mass loss term. Solid curve #2 has $\bar{M}=1.0$ and $\bar{\rho}=\infty$. Solid curve #3 has $\bar{M}=0$ and $\bar{\rho}=0.025$. We see that in each of these cases, the droplet lifetime is increased from the $\bar{C}=0$ case.

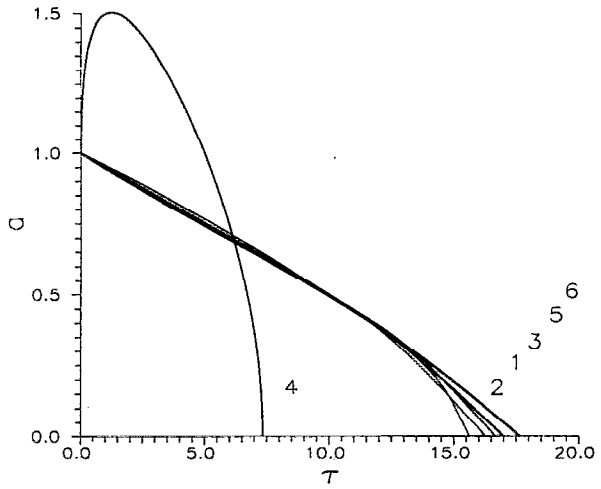

FIG. 8. Zero capillary number, unsteady spreading, and evaporation: $a(\tau)$ vs τ showing the effect of contact-angle hysteresis. In each case $\bar{C}=0$, $\bar{E}=0.1$, $K=1.0$, $\bar{\eta}=1.0$, and $m=3$. Again note that when $\bar{C}=0$ the droplet profile is independent of slip, Marangoni effects, and vapor recoil. The values of Θ_R and Θ_A are (1) $\Theta_R=\Theta_A=1.8$; (2) $\Theta_R=1.2$, $\Theta_A=1.8$; (3) $\Theta_R=1.8$, $\Theta_A=2.2$; (4) $\Theta_R=\Theta_A=0.2$; (5) $\Theta_R=\Theta_A=2.0$; (6) $\Theta_R=\Theta_A=2.2$. The numbering indicates the ordering of the curves along the bottom of the figure. The disappearance time decreases when the region where spreading is present is larger. Curves #1 and #2 show that when Θ_A is fixed while Θ_R is decreased, evaporation is promoted. Note that while the contact-line position is momentarily larger when hysteresis is present (curve #2) owing to the less mobile contact line, due to the subsequent decrease in the contact angle (see Fig. 9) when hysteresis is present, $a(\tau)$ is eventually driven more rapidly to zero.

are discussed in the next section). Although the droplet ultimately disappears, we now see that initially the droplet spreads (Fig. 6). The contact angle in this case decreases monotonically (Fig. 7). Again we note the presence of a contact-angle plateau; this value is roughly 1.4 while the steady value, Θ_S, for these parameter values given by Eq. (20) is 1.57.

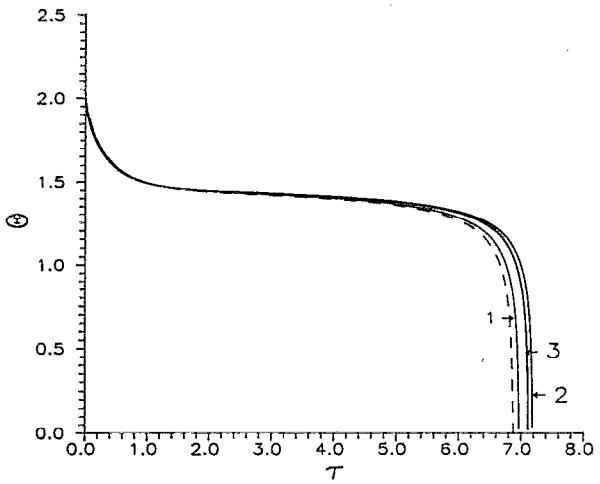

FIG. 7. Small capillary number, unsteady spreading, and evaporation: $\Theta(\tau)$ vs τ corresponding to Fig. 6. Here $\bar{E}=0.05$, $K=0.1$, $\bar{\eta}=0.1$, $\Theta_R=\Theta_A=0.1$, and $m=3$. The dashed curve corresponds to $\bar{C}=0$ and shows that Θ decreases monotonically. However, there still is a region in which Θ remains nearly constant. Again, this constant value is approximately Θ_S, the angle which is obtained by a balance of viscous spreading and evaporative effects at the contact line. The solid curves marked #1, #2, and #3 correspond to those in Fig. 6 having the same parameter values. We see that in each case, the effect of these terms is to delay evaporation.

We now consider the effects of contact-angle hysteresis. We have looked at a wide variety of cases corresponding to different values of Θ_A and Θ_R with and without contact-angle hysteresis. These include cases with initial contact angle in three different regimes; $\Theta(0)>\Theta_A$, $\Theta_R<\Theta(0)<\Theta_A$, and $\Theta(0)<\Theta_R$. Results from typical cases are shown in Figs. 8 and 9. Here $\bar{E}=0.1$, $K=1.0$, $\bar{\eta}=1.0$, and $m=3$, while Θ_R and Θ_A vary. In particular, we shall examine the effect of the values of Θ_R and Θ_A on the droplet lifetime. We shall consider situations where a hysteresis region is introduced (imagine starting from a case with $\Theta_R=\Theta_A$) by (i) decreasing Θ_R and keeping Θ_A fixed, and (ii) increasing Θ_A and keeping Θ_R fixed.

(i) In this situation, the introduction of a hysteresis region means that the droplet is less likely to recede (in fact, if $\Theta_R=0$ the only tendency for the droplet radius to decrease is due to evaporative mass loss). Receding leads to "thicker" drops, or larger contact angles (compare curve #1 with curve #2 in Fig. 9) and hence weaker mass flux. Therefore, when a drop is less likely to recede, mass flux is enhanced. While $a(\tau)$ is temporarily larger for drops with hysteresis due to the relative immobility of the contact line, $\Theta(\tau)$ gets smaller and smaller and the dominant contribution at the contact line is the mass loss, which eventually drives $a(\tau)$ to zero faster in the hysteresis case. As a result, the droplet lifetime is *decreased* when Θ_A is fixed and Θ_R is decreased from Θ_A.

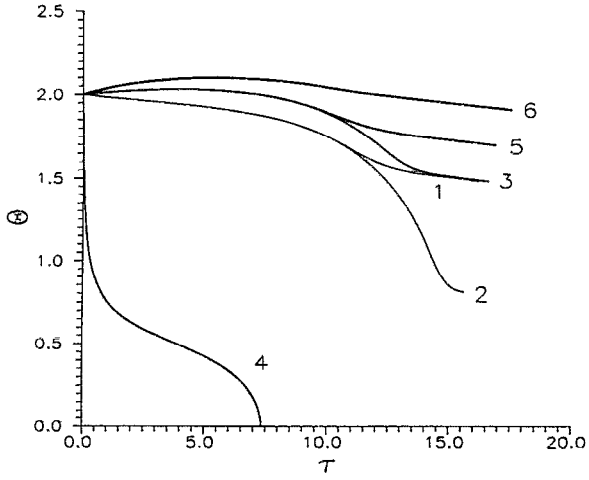

FIG. 9. Zero capillary number, unsteady spreading, and evaporation: $\Theta(\tau)$ vs τ corresponding to $a(\tau)$ in Fig. 8. The parameter values are the same as indicated in Fig. 8.

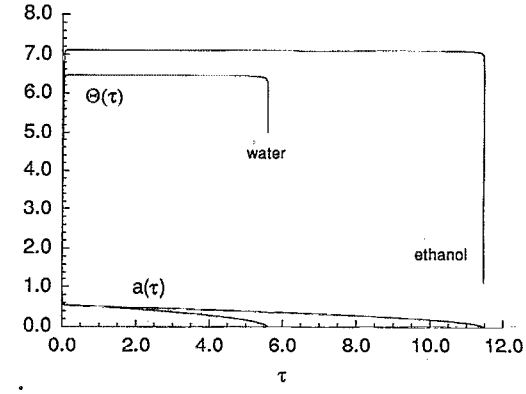

FIG. 10. Zero capillary number, unsteady spreading, and evaporation: $a(\tau)$ and $\Theta(\tau)$ vs τ for two different physical systems: water and ethanol. The parameter values for water are $\bar{E}=0.1$, $K=0.002$, $\bar{\eta}=0.03$, $\Theta_R=\Theta_A=0.1$, and $m=3$. The parameter values for ethanol are $\bar{E}=0.049$, $K=0.001$, $\bar{\eta}=0.02$, $\Theta_R=\Theta_A=0.1$, and $m=3$. We used $\bar{C}=0$ in both cases. Again note that when $\bar{C}=0$ the droplet profile is independent of slip, Marangoni effects, and vapor recoil. Except for the initial and final stages, the contact angle stays at a nearly constant value. This equilibrium value for the contact angle, which is given by Eq. (20) and represents a balance between viscous spreading effects and evaporative effects, is predicted to be 6.5 for water and 7.1 for ethanol.

(ii) In this situation, the introduction of a hysteresis region means that the droplet is less likely to spread. Spreading leads to thinner drops, or smaller contact angles (compare curve #1 and curve #3 in Fig. 9), and hence enhanced mass flux. Therefore, when a drop is less likely to spread, mass flux is suppressed. So here the effect is reversed; the droplet lifetime is *increased* when Θ_R is fixed and Θ_A is increased from Θ_R.

These cases demonstrate that effects which tend to decrease the contact angle and thin the drop, decrease the droplet lifetime, while effects which tend to increase the contact angle and contract the drop, increase the droplet lifetime.

The other curves in Figs. 8 and 9 show results for $\Theta_R=\Theta_A=0.2$ (curve #4), $\Theta_R=\Theta_A=2.0$ (curve #5), and $\Theta_R=\Theta_A=2.2$ (curve #6). Consistent with the above conclusions we find that when the tendency to spread is stronger, complete evaporation is promoted (see Fig. 8); it is clear from Fig. 9 that drops with smaller values of Θ disappear sooner. Finally, we note that hysteresis is a small effect when Θ_R and Θ_A are small compared to the initial value of Θ since for most of the droplet lifetime $\Theta>\Theta_A$ and hysteresis does not play a role.

A related feature that we can see in Fig. 9 is that the contact angle, Θ_D, at the moment of disappearance (i.e., corresponding to $a=0$) varies strongly from case to case. Equations (24) and (14) can be written for small values of a,

$$a\frac{d\Theta}{d\tau}=-\left(\frac{\bar{E}}{K}+2\Theta\bar{\eta}f(\Theta)\right), \tag{26a}$$

$$\Theta\frac{da}{d\tau}=-\left(\frac{\bar{E}}{K}+\Theta\bar{\eta}f(\Theta)\right). \tag{26b}$$

Bounded time derivatives of Θ requires that as $a\to 0$ the quantity on the right-hand side of Eq. (26a) vanish. However, this is only possible if $f(\Theta_D)<0$, so that

$$\frac{\bar{E}}{K}-2\bar{\eta}\Theta_D|\Theta_R-\Theta_D|^m=0. \tag{27}$$

Positive, real solutions to this equation give the final contact angle, Θ_D. Note that this result depends on Θ_R but not on Θ_A. We find that this result agrees with the numerically calculated results in Fig. 9 which have $\Theta_D\neq 0$. However, positive real solutions, Θ_D do not exist for all parameter values. In such cases, both a and Θ are proportional to $(\tau_D-\tau)^{1/2}$ as $\tau\to\tau_D$ so that $\Theta_D=0$, but the time derivatives of a and Θ are infinite at $\tau=\tau_D$. Curve #4 in Fig. 9 corresponds to such a case. Equation (27) shows that this behavior is more common for small values of Θ_R. We note that in principle, our assumption of a quasisteady solution breaks down when time derivatives become infinite. However, our analysis should be asymptotically valid for any nonzero a.

We now turn to the first case shown in Table II. Since $\bar{C}^{-1}$ is much larger than any other parameter listed for both water and ethanol, we shall discuss the results in this case obtained with $\bar{C}=0$. Figure 10 shows plots of $a(\tau)$ and $\Theta(\tau)$ for water and for ethanol. Here we see that for both systems there is a rapid readjustment of the contact line and the contact angle from the initial conditions. The value of Θ attains a plateau, at a value much greater than Θ_A, over the entire range with the exception of the initial and final stages. In fact, this value is nearly that predicted by Eq. (20) which gives $\Theta_S=6.5$ for water and $\Theta_S=7.1$ for ethanol. The presence of this plateau is related to the smallness of K.

To get a further understanding of these results we analyze the system of Eqs. (14) and (24) in the limit as $K\to 0$. The details of this analysis are found in Anderson.[20] As suggested by the plots of a and Θ vs τ in Fig. 10, we find that the solution to Eqs. (14) and (24) in the limit of $K\to 0$ corresponds to multiple layers in time. From this analysis we also obtain an estimate for the disappearance time.

There is an initial, or inner layer, near $\tau=0$, of $O(K)$ where the contact line adjusts rapidly due to the large evaporation rate at the contact line (see Fig. 10). Here, viscous spreading effects are negligible to leading order. Furthermore, there is no bulk mass loss to leading order.

There is a second layer in time of $O(K^{(2m+1)/2(m+1)})$ similar to the first layer in that there is negligible leading-order bulk mass loss. However, now due to the increased value of the contact angle, viscous spreading effects combine with evaporative effects at the contact line to slow the rate of increase of the contact angle.

This intermediate layer is followed by an $O(1)$ layer in time where viscous spreading effects have now balanced the evaporative effects at the contact line. That is, the initial rapid increase of the contact angle (and decrease of the droplet radius) has been stopped by viscous spreading effects, which favor a smaller value of the contact angle. The value of Θ is $O(K^{-1/(m+1)})$ (i.e., large), corresponding to the constant contact angle Θ_S satisfying Eq. (20), and the value of a is $O(K^{1/2(m+1)})$. Once again, this layer has negligible leading-order bulk mass loss.

The fourth layer corresponds to a long time scale, $O[1/(K^{1/(m+1)}|\ln K|)]$. This represents the time scale on which bulk mass loss is significant when the contact angle remains at the above (large) constant value, Θ_S. The large contact angle leads to less efficient evaporation and hence the long time before a significant amount of mass evaporates. The behavior in this regime corresponds to bulk evaporation of the droplet with a constant contact angle. Motion at the contact line is due only to mass loss in the bulk. The decrease of the droplet radius is approximately square-root in time. It is this time scale that measures the disappearance time, τ_D, given by

$$\tau_D=\frac{4(m+1)}{3(2m+3)}\frac{\Theta_{S0}}{\bar{E}}\left\{1-\frac{1}{|\ln K|}\frac{2(m+1)}{2m+3}\left[\ln(2\Theta_{S0})+\Theta_{S0}\ln\left(\frac{2}{\Theta_{S0}}\right)-1\right]\right\}\frac{1}{K^{1/(m+1)}|\ln K|}, \tag{28}$$

where $\Theta_{S0}=(\bar{E}/\bar{\eta})^{1/(m+1)}$. Recall that the scaling unit for τ_D is a slow viscous time scale, so that, as expected, the final time increases with decreasing $\bar{E}$ ($\tau_D\sim\bar{E}^{-m/(m+1)}$). Furthermore, it increases with decreasing $\bar{\eta}$ ($\tau\sim\bar{\eta}^{-1/(m+1)}$). This can also be expected if we note that when $\Theta>\Theta_A$ the increasing of $\bar{\eta}$ corresponds to stronger spreading, and hence thinning of the drop, which promotes evaporation. This estimate for the disappearance time agrees well with the numerical results for water and ethanol plotted in Fig. 10.

The corresponding disappearance times in dimensional terms for the first case shown in Table II (and Fig. 10) are 230 s for ethanol and 187 s for water. This nonintuitive result that water evaporates before ethanol might be explained in a number of ways. First, the disappearance time depends on η, the value for which we do not know precisely. Another factor to bear in mind is that the base temperature for ethanol is considerably lower than that for water. That is, the base temperature is taken to be ten degrees above the saturation temperature in each case (so $T_B=89$ °C for ethanol while $T_B=110$ °C for water). We find that if the base temperature for the ethanol system is taken to be the same as that for water, the ethanol droplet does in fact evaporate first. We discuss this issue further in Sec. VI C.

B. Small capillary number

Consider Eqs. (9), (14), and (15) with $\bar{C}\ll 1$ but nonzero with all other parameters $O(1)$. In order to solve Eq. (9) in this limit subject to the boundary conditions (13) we assume

$$h=h_0+\bar{C}h_1+\cdots. \tag{29}$$

In general, we must expand a and Θ as well. However, this can be avoided since h can be determined in terms of a and Θ before the contact-line and global mass balance conditions are enforced. We find that this leads to an $O(\bar{C}^2)$ error made in computing h_1 but this is acceptable since we are only interested in the solution through $O(\bar{C})$.

At leading order we find

$$h_0=\frac{\Theta}{2a}(a^2-x^2). \tag{30}$$

At $O(\bar{C})$ we find

$$h_{1xxx}=\frac{1}{h_0^2(\beta+\frac{1}{3}h_0)}\int_x^a\left(h_{0\tau}+\frac{\bar{E}}{K+h_0}\right)dx-\frac{2\bar{E}^2}{\bar{\rho}}\left(\frac{h_{0x}}{(K+h_0)^3}\right)-\bar{M}K\left(\frac{h_{0x}(\beta+\frac{1}{2}h_0)}{h_0(K+h_0)^2(\beta+\frac{1}{3}h_0)}\right) \tag{31}$$

subject to $h_1(a,\tau)=0$, $h_{1x}(a,\tau)=0$, and $h_{1x}(0,\tau)=h_{1xxx}(0,\tau)=0$. Note that the second symmetry condition is satisfied if

$$\int_0^a\left(h_{0\tau}+\frac{\bar{E}}{K+h_0}\right)dx=0. \tag{32}$$

However, we replace h_0 by h and enforce

$$\int_0^a\left(h_\tau+\frac{\bar{E}}{K+h}\right)dx=0. \tag{33}$$

This means that there will be an acceptable $O(\bar{C}^2)$ error made in calculating h_1.

We can integrate Eq. (31) to obtain a solution for h_1 (see Appendix A). The global mass balance with the expansion for h correct to $O(\bar{C})$ inserted gives a relation between $a(\tau)$ and $\Theta(\tau)$. Together with the contact-line condition (14) this gives an evolutionary system for $a(\tau)$ and $\Theta(\tau)$ subject to initial conditions. We solved this system using a Runge–Kutta scheme (IMSL routine DIVPRK) with integrals from the global mass balance condition also computed numerically (IMSL routines DQDAGS and DTWODQ).

Figures 4 and 5 show the solutions for a and Θ which include corrections due to the unsteady and mass loss terms, thermocapillarity, and vapor recoil, using $\bar{C}=0.1$, $K=0.1$, $\bar{\eta}=0.1$, $\Theta_R=\Theta_A=0.1$, $m=3$, $\beta=0.5$, and $\bar{E}=0.5$ (this is the strong evaporation regime with no contact-angle hysteresis present). Curve #1 shows just the effect of the unsteady

and mass-loss terms ($\bar{M}=0$, $\bar{\rho}=\infty$). While the basic behavior of a and Θ is similar to the $\bar{C}=0$ case (dashed curves), we find that the disappearance time is increased. Curve #2 shows the result with the unsteady and mass loss terms as well as the Marangoni term ($\bar{M}=1.0$, $\bar{\rho}=\infty$). Here we see that the droplet lifetime is prolonged slightly. Curve #3 shows the results including the unsteady and mass loss term with the vapor recoil term ($\bar{M}=0$, $\bar{\rho}=10$). Again, the effective evaporation rate decreases.

Another case is shown in Figs. 6 and 7. These correspond to the weak evaporation regime. The solid curves, corresponding to $\bar{C}=0.1$, are similar to the $\bar{C}=0$ results (dashed curves) and again show that the most significant effect of the correction terms is to increase the lifetime of the droplet. The unsteady and mass loss terms (solid curve #1 with $\bar{M}=0$, and $\bar{\rho}=\infty$) increase the droplet lifetime. The inclusion of the vapor recoil term (solid curve #3 with $\bar{M}=0$, and $\bar{\rho}=0.025$) and the Marangoni term (solid curve #2 with $\bar{M}=1.0$, and $\bar{\rho}=\infty$) increase the droplet lifetime further.

We now wish to describe physically the effects seen in these results. We first note that in the limit $\bar{C}\to 0$, evaporation is strongly affected by the behavior at the contact line. From Eq. (11) we know that the mass flux is strongest where the droplet is thinnest; that is, at or near the contact line. Therefore, mechanisms which tend to increase Θ *increase* the droplet lifetime while those which tend to decrease Θ *decrease* the droplet lifetime.

We find that the inclusion of the unsteady and mass loss terms in the correction h_1 increases the droplet lifetime. This seems counterintuitive since if more mass is lost one might expect the droplet lifetime to be decreased. However, the combined effect on the *droplet profile* is to transport mass from the contact-line region toward the center of the drop. As a result the drop steepens near the base, increasing the contact angle, making evaporation less efficient.

We now consider thermocapillary effects. Thermocapillarity results from surface-tension gradients on the droplet interface. Since the interface temperature is lower at the top of the droplet than it is near the contact line, thermocapillarity drives a flow away from the contact line along the interface, down near the center of the drop, and outward along the base. The return flow is generated by a pressure gradient in which the pressure near the center of the droplet is high, causing the drop to thicken near the center (Ehrhard and Davis[7]). Consequently the droplet lifetime is increased.

We now consider vapor recoil. Vapor recoil effectively causes an increased pressure to be exerted on the droplet due to momentum transfer from the escaping particles. As described in Palmer[12] and Burelbach, Bankoff, and Davis,[9] a slowly moving liquid particle undergoes a large acceleration upon vaporization owing to the disparate densities between the vapor and liquid phases and exerts a pressure downward on the interface. Since the mass flux is larger near the contact line than near the center of the droplet, the pressure is correspondingly stronger near the contact line. Thus, this nonuniform pressure distribution causes the drop to "stand up," retarding evaporation.

C. "Large" capillary number

We now consider Eqs. (9), (14), and (15) with $\bar{C}\gg 1$. We introduce an evaporative time scale, $t=\bar{E}\tau$, and neglect thermocapillary and vapor recoil effects to obtain the evolution equation,

$$h_t+\frac{1}{K+h}+\lambda\frac{\partial}{\partial x}\left[h^2\left(\beta+\frac{1}{3}h\right)h_{xxx}\right]=0, \tag{34}$$

the contact-line condition,

$$a_t(t)=-\frac{1}{K\Theta(t)}+\frac{\bar{\eta}}{\bar{E}}f(\Theta(t)), \tag{35}$$

and the global mass balance,

$$\int_0^{a(t)}\left(h_t(x,t)+\frac{1}{K+h(x,t)}\right)dx=0. \tag{36}$$

More specifically, we shall consider $\lambda\equiv\bar{C}^{-1}/\bar{E}\ll 1$. Furthermore, the ratio, $\bar{\eta}/\bar{E}$, which is the coefficient of the viscous spreading in Eq. (35), will be taken small. In the limit $\lambda\to 0$ the spatial derivatives drop out of the evolution equation (34) and therefore we expect the drop to have a shape given by the initial conditions near the center and some type of boundary-layer correction near the contact line, where the spatial derivatives cannot be neglected. Before proceeding with inner and outer expansions for h we note that when $\lambda=0$ and $\bar{\eta}/\bar{E}=0$, we obtain

$$h_t+\frac{1}{K+h}=0, \tag{37}$$

$$a_t(t)=-\frac{1}{K\Theta(t)}. \tag{38}$$

The global mass balance (36) is identically satisfied when Eq. (37) holds. Now if we enforce boundary conditions (13a) and (13b) on h we find that Eq. (38) is identically satisfied. Therefore, a solution of Eq. (37) is the exact solution when $\lambda=0$ and $\bar{\eta}/\bar{E}=0$ with a and Θ determined by the boundary conditions (13a) and (13b) [or equivalently related by Eq. (38)]. These solutions represent motion purely due to evaporation. The following analysis represents a perturbation from this purely evaporating solution, where $\lambda\ll 1$ and $\bar{\eta}/\bar{E}\ll 1$.

For an outer solution we seek a regular perturbation expansion in powers of λ. We expect that the contact-line position will be determined by evaluating the outer solution at $x=a(t)$ and therefore use a strained coordinate[24] in time to obtain corrections to the leading-order solution for a and Θ. We expand the variable as follows:

$$h=h_0(x,s)+\lambda h_1(x,s)+\cdots, \tag{39a}$$

$$a=a_0(s)+\lambda a_1(s)+\cdots, \tag{39b}$$

$$\Theta=\Theta_0(s)+\lambda\Theta_1(s)+\cdots, \tag{39c}$$

with the strained coordinate $t=s+\lambda t_1(s)+\cdots$. At leading order we obtain from the evolution equation (34)

$$\frac{\partial h_0}{\partial s}+\frac{1}{K+h_0}=0. \tag{40}$$

We solve this subject to the initial profile condition $h(x,0)=1-x^2$ and find that

$$h_0(x,s)=[(1-x^2+K)^2-2s]^{1/2}-K. \tag{41}$$

At $O(\lambda)$ we find that

$$\frac{\partial h_1}{\partial s}-\frac{h_1}{(K+h_0)^2}=t_1'(s)\,\frac{\partial h_0}{\partial s}-\frac{\partial}{\partial x}\left[h_0^2\left(\beta+\frac{1}{3}h_0\right)h_{0xxx}\right]. \tag{42}$$

The solution, h_1, which is given in Appendix B, depends on the presently undetermined function $t_1(s)$.

We next consider the inner region. Here we introduce a stretched variable, $\xi=[a(t)-x]/\lambda$, and a scaled profile height, $H=h/\lambda$, to obtain

$$\lambda H_t+a_t H_\xi+\frac{1}{K+\lambda H}=-\left[H^2 H_{\xi\xi\xi}\left(\beta+\frac{1}{3}\lambda H\right)\right]. \tag{43}$$

We expand $H=H_0+\lambda H_1+\cdots$ and find that the leading-order problem can be integrated once giving

$$d_1(s)+a_{0s}H_0+\frac{\xi}{K}=-\beta H_0^2 H_{0\xi\xi\xi} \tag{44}$$

subject to the boundary conditions $H_0(0)=0$ and $H_{0\xi}(0)=\Theta_0$. Here $d_1(s)$ is an unknown function of time arising as an integration constant. The left-hand side of this equation corresponds to the unsteady and mass loss terms while the right-hand side corresponds to the slip term.

Before the inner problem can be solved, we must determine the matching conditions. Expecting that as $\xi\to\infty$ (i.e., away from the contact line), $H_{0\xi\xi\xi}\to 0$, we find that matching at leading order requires that $h_0(a_0,s)=0$. Since h_0 contains no unknown quantities, this gives an expression for the leading-order contact-line position

$$a_0^2=1+K-(K^2+2s)^{1/2}. \tag{45}$$

This immediately shows that the drop radius decreases monotonically in time to leading order; evaporation is the dominant mechanism controlling the motion of the contact line. Matching at $O(\lambda)$ gives

$$d_1(s)=a_{0s}[a_1(s)h_{0x}(a_0,s)+h_1(a_0,s)]. \tag{46}$$

This equation relates two unknown quantities, $d_1(s)$ and $a_1(s)$ and also involves $t_1(s)$ through h_1.

Now, since a_0 is known explicitly, the contact-line condition (35) determines Θ_0. If we now expand Θ_0 in powers of $\bar{\eta}/\bar{E}$, we find that

$$\Theta_0=\Theta_{00}-\frac{\bar{\eta}}{\bar{E}}\,[K\Theta_{00}^2 f(\Theta_{00})]+O\left(\frac{\bar{\eta}}{\bar{E}}\right)^2, \tag{47}$$

where $\Theta_{00}=-(Ka_{0s})^{-1}$. Note that a_{0s} is always negative. We assume, for proper ordering, that $1\gg\bar{\eta}/\bar{E}\gg\lambda$.

Now, to solve the inner problem we write

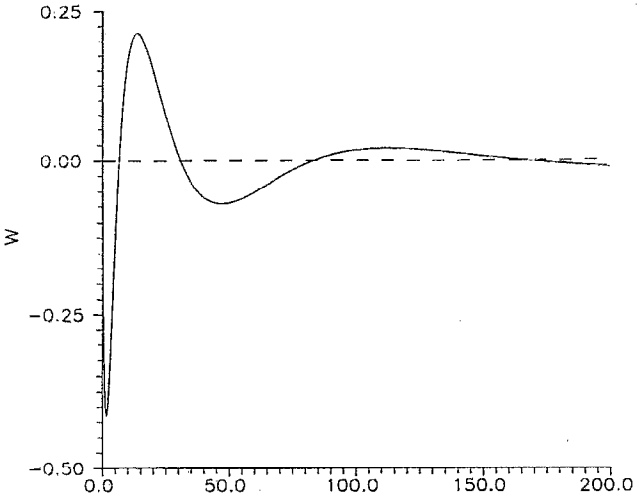

FIG. 11. Large capillary number, unsteady spreading, and evaporation: the inner solution $w(\zeta)$. The solution shows an oscillatory behavior of the profile in the inner region. The scaled inner shape profile is $W=\beta K^2\Theta_{00}^5 f(\Theta_{00})w$ and the scaled inner coordinate is $\xi=\beta K\Theta_{00}^3\zeta$. When $f(\Theta_{00})$ is positive (negative) the inner solution has a slight dip (bulge) near the contact line. If $f(\Theta_{00})=0$ there is no contribution from the inner solution at this order and the outer solution is the uniformly valid solution.

$$H_0=H_{00}(\xi)+\frac{\bar{\eta}}{\bar{E}}\,W(\xi)+\cdots. \tag{48}$$

Inserting this into the $O(1)$ inner equation (44) gives at leading order in $\bar{\eta}/\bar{E}$ the same equation with H_0 replaced by H_{00}; however, now the boundary condition $H_{00\xi}(0)=\Theta_{00}$ is such that a solution linear in ξ is allowed, viz.,

$$H_{00}=-\frac{\xi}{Ka_{0s}}=\Theta_{00}\xi, \tag{49}$$

where we have also imposed $H_{00}(0)=0$ giving $d_1(s)=0$. We shall find that this expression is the same as the first nonzero term in the outer solution expanded near $x=a$.

We next consider the $O(\bar{\eta}/\bar{E})$ inner problem. Here we obtain

$$w=\zeta^2 w_{\zeta\zeta\zeta} \tag{50}$$

subject to

$$w(0)=0, \tag{51a}$$

$$w_\zeta(0)=-1, \tag{51b}$$

and the matching condition

$$w_{\zeta\zeta\zeta}\to 0, \quad \text{as } \zeta\to\infty, \tag{51c}$$

where $W=\beta K^2\Theta_{00}^5 f(\Theta_{00})w$ and $\xi=\beta K\Theta_{00}^3\zeta$. This rescaling leaves the new inner variables, w and ζ, independent of time. As a result, we need only solve this equation once; the solutions at different times simply change the amplitude and stretch the coordinate. We have solved this equation numerically and the solution is shown in Fig. 11. Here we see that the solution is oscillatory and decays at infinity. Equation (50) represents a balance between the slip/capillary term $(\beta H^2 H_{\xi\xi\xi})_\xi$ and the unsteady motion of the contact line

$a_t H_\xi$ in Eq. (43). Since W is proportional to $f(\Theta_{00})$ the oscillations are directly related to the contact angle being one which leads to viscous spreading (or receding). We note here that similar oscillatory shapes near contact lines have been found in different contexts. Keller and Miksis[25] (and more recently Lawrie[26]) considered potential flow in a liquid wedge and calculated similarity shapes in which the adjustment of the initial contact angle to the equilibrium contact angle led to capillary waves on the free surface. We note that while $w_{\zeta\zeta\zeta}$ decays to zero "quickly" as $\zeta\to\infty$, the decay of $w(\zeta)$ is much weaker due to the factor of ζ^2 in Eq. (50). Also, the sign of W depends on the sign of $f(\Theta_{00})$. If $f(\Theta_{00})>0$ oscillations start out as a slight dip near the contact line and if $f(\Theta_{00})<0$ the oscillations start out as a slight bulge near the contact line. Again, if $f(\Theta_{00})=0$ (i.e., the contact angle corresponds to an equilibrium angle in the nonvolatile case) there are no oscillations, and to this order, the outer solution is the uniformly valid solution. Note that decreasing β decreases the amplitude and also the range in x. Also, larger Θ_{00} implies a larger amplitude and a greater influence of the inner region toward the center of the drop. That is, the inner region has a more significant effect on the profile as a whole as the contact angle increases.

We now return to the matching condition (46) with $d_1(s)=0$ and find that $a_1(s)$ is proportional to $h_1(a_0,s)$. Recalling that h_1 depends on the strained coordinate function $t_1(s)$, this formula suggests choosing $t_1(s)$ such that $h_1(a_0,s)=0$ and therefore $a_1(s)=0$. Such a choice of $t_1(s)$ builds the $O(\lambda)$ correction to the contact-line position into the leading-order solution, $a_0(s)$, through the coordinate transformation [the specific form for $t_1(s)$ is given in Appendix B].

Now, from the contact-line condition (35), using the fact that $a_1=0$, we find that

$$\Theta_1=-K\Theta_{00}^2 t_1'(s)a_{0s}+O\left(\frac{\bar{\eta}}{\bar{E}}\right). \tag{52}$$

Finally, we can write down a uniformly valid solution for the droplet profile

$$h_{\text{unif}}=[h_0(x,s)+\lambda h_1(x,s)]+\lambda\left(\frac{\bar{\eta}}{\bar{E}}\,\beta K^2\Theta_{00}^5 f(\Theta_{00})w(\zeta)\right)+\cdots. \tag{53}$$

While the inner and outer solutions match, as a result of the relatively slowly decaying nature of the inner solution, realistic solutions obtained from this equation require that λ be small enough so that the inner solution does not alter the outer profile. The global mass balance (36) must be applied to a uniformly valid solution, and is found to be satisfied identically though $O(\lambda^2)$ by Eq. (53).

From this analysis we can also obtain an estimate for the disappearance time. This is found by setting a_0 in Eq. (45) equal to zero. In terms of the time coordinate, s, we find that

$$s_D=\frac{1+2K}{2}. \tag{54}$$

This simple relationship shows the dependence on the nonequilibrium parameter, K. For a highly volatile drop ($K\to 0$) the disappearance time is smallest, while for a nonvolatile drop ($K\to\infty$) the droplet never disappears. In terms of the strained coordinate and the slow viscous time scale used in Eq. (28) we find that

$$\tau_D=\frac{1+2K}{2\bar{E}}+\frac{\lambda}{\bar{E}}\,t_1(s_D). \tag{55}$$

Here, $\tau_D\sim\bar{E}^{-1}$ while in the previous result for $\bar{C}=0$ and $K\ll 1$ given by Eq. (28) we found $\tau_D\sim\bar{E}^{-m/(m+1)}$.

In dimensional terms, the leading-order estimates for the disappearance times are 9.4 s for ethanol and 8.7 s for water. Again we see the apparent paradox that water evaporates before ethanol. However, the base temperature is considerably lower for ethanol than that for water and, again, we find that ethanol evaporates before water if the base temperatures in each case are taken to be the same. We note that the present time estimates, at least to leading order, do not involve any contact-line effects. The time scale for evaporation is determined directly by a balance of heat conduction with the latent heat of vaporization. Finally, we note that the dimensional disappearance times for $\epsilon=0.1$ (the first example shown in Table II, corresponding to a thin drop) are much greater than those for $\epsilon=0.005$ (the second example shown in Table II, corresponding to a *very* thin drop), as expected. This could be another resolution to the above paradox. That is, if a more realistic situation for an ethanol drop is that it is initially thinner than a water drop on the same substrate, then this too would reduce the evaporation time for ethanol.

We observe that the parameter K is the only one that appears in the leading-order results. In the following we discuss the leading-order and correction terms for different values of K with the other parameters fixed ($\beta=0.001$, $\bar{E}=1.0$, $\Theta_R=\Theta_A=2.0$, and $m=3$).

Figures 12–14 show results for $K=1.0$ and different values of λ and η. Figure 12 shows the monotonic decrease in the droplet radius. We see that when λ is perturbed from

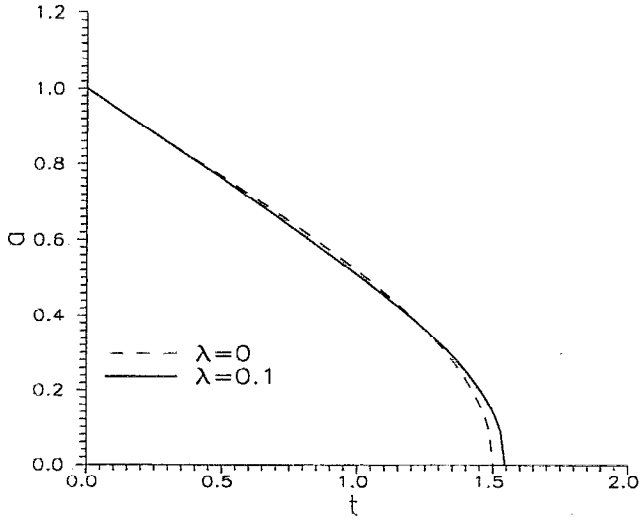

FIG. 12. Large capillary number, unsteady spreading, and evaporation: $a(t)$ vs t for $K=1.0$, $\beta=0.001$, $\bar{E}=1.0$, $\Theta_R=\Theta_A=2.0$, and $m=3$. Curves for $\lambda=0$ (dashed) and $\lambda=0.1$ (solid) are shown. Here we see that the droplet lifetime is prolonged as λ is increased from zero.

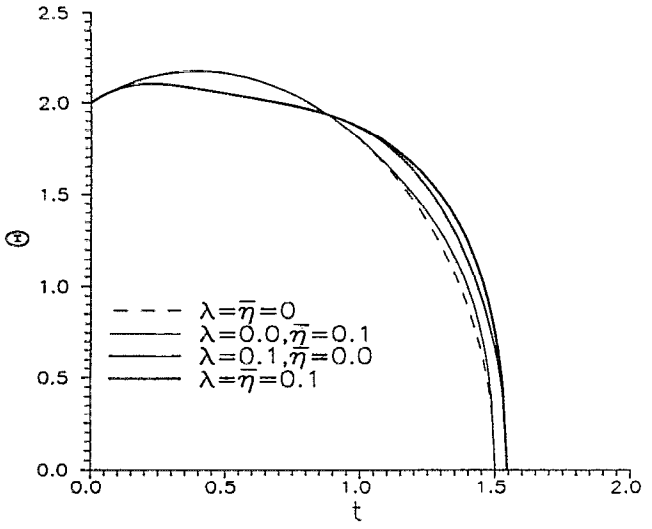

FIG. 13. Large capillary number, unsteady spreading, and evaporation: $\Theta(t)$ vs t for $K=1.0$, $\beta=0.001$, $\tilde{E}=1.0$, $\Theta_R=\Theta_A=2.0$, and $m=3$. The dashed curve corresponds to $\lambda=\bar{\eta}=0$. We see that a nonzero value of $\bar{\eta}$ alters the profile but does not change the final time. A nonzero value of λ leads to a decrease in Θ at early times and an increase in Θ for later times (relative to the unperturbed case) and an overall increase in the droplet lifetime.

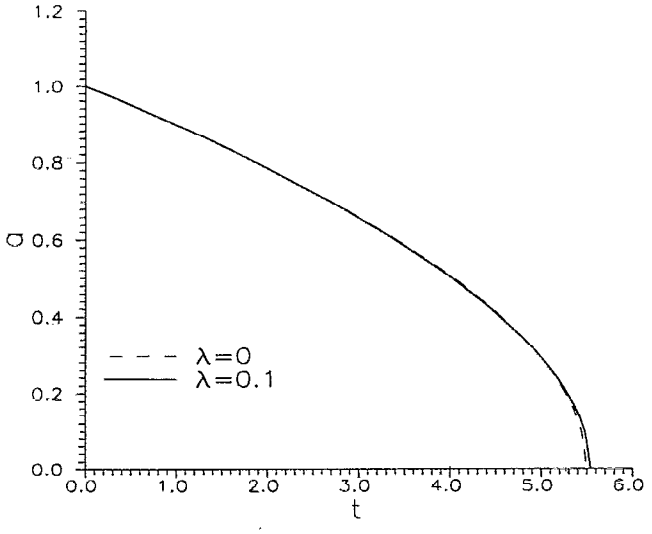

FIG. 15. Large capillary number, unsteady spreading, and evaporation: $a(t)$ vs t for $K=5.0$, $\beta=0.001$, $\tilde{E}=1.0$, $\Theta_R=\Theta_A=2.0$, and $m=3$. Curves for $\lambda=0$ (dashed) and $\lambda=0.1$ (solid) are shown. We note that the effect of the correction term in λ is to slightly prolong the droplet life, while changes in $\bar{\eta}$ do not change the droplet lifetime, nor the value of a.

zero, the droplet lifetime is prolonged. Note that the value of a, and hence the disappearance time, is independent of $\bar{\eta}$. This reflects the fact that the contact-line position is determined to this order by the *outer* solution. Figure 13 shows the changes in Θ that occur when λ and $\bar{\eta}$ are perturbed from zero. Here we see that changing $\bar{\eta}$ alone changes the value of Θ but, again, does not affect the disappearance time. Relative to the unperturbed case, there is an initial decrease in Θ followed by an eventual increase. Figure 14 shows the profiles for the case $\lambda=\bar{\eta}=0.1$ at four different times. Note that no oscillatory behavior is observable on this scale.

Next, we consider a larger value of K. Figures 15–17 correspond to $K=5.0$ and different values of λ and $\bar{\eta}$. Figure 15 shows the droplet radius, $a(t)$. Here we see that correction terms due to nonzero λ have a very small effect in prolonging the droplet lifetime (the dashed curve corresponds to $\lambda=0$). In Fig. 16 we see that when $\lambda=\bar{\eta}=0$ (dashed curve) the contact angle decreases monotonically in time. When correction terms are included due to nonzero λ only, the contact angle changes only slightly. However, when a nonzero value of $\bar{\eta}$ is used, the contact angle, while still decreasing monotonically, is significantly larger for later times. Fig-

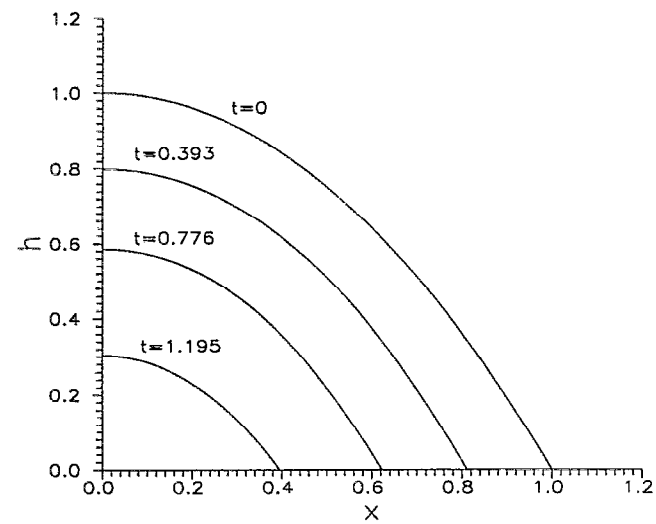

FIG. 14. Large capillary number, unsteady spreading, and evaporation: Uniform profiles for $K=1.0$, $\beta=0.001$, $\tilde{E}=1.0$, $\Theta_R=\Theta_A=2.0$, $m=3$, and $\lambda=\bar{\eta}=0.1$. Consistent with the results shown in Fig. 13 the contact angle tends to decrease from its initial value. Here we also see that there is no noticeable effect of the oscillatory behavior in the inner region.

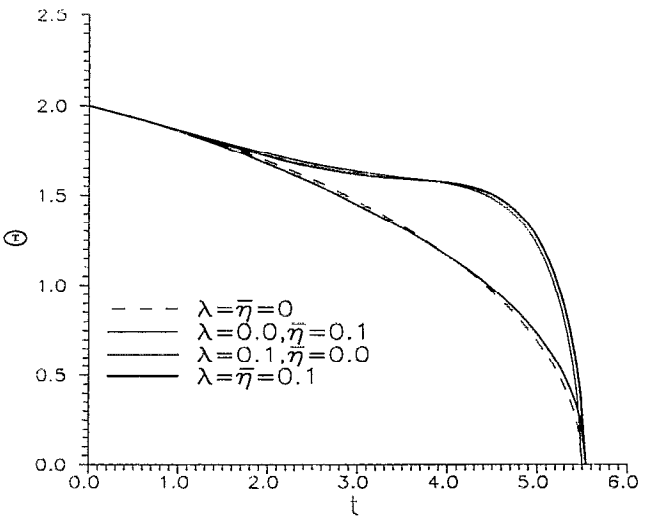

FIG. 16. Large capillary number, unsteady spreading, and evaporation: $\Theta(t)$ vs t for $K=5.0$, $\beta=0.001$, $\tilde{E}=1.0$, $\Theta_R=\Theta_A=2.0$, and $m=3$. The dashed curve corresponds to $\lambda=\bar{\eta}=0$. Here the contact angle decreases monotonically in time in all cases shown. We see a significant departure in the value contact angle from the unperturbed case when $\bar{\eta}$ is perturbed from zero. Relatively small changes occur when only λ is perturbed from zero.

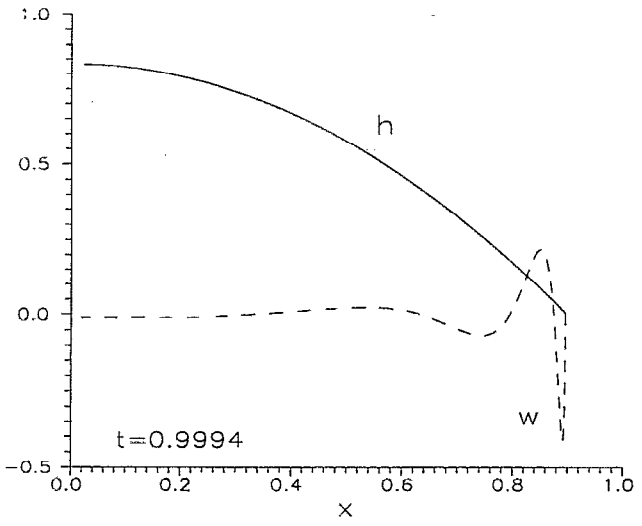

FIG. 17. Large capillary number, unsteady spreading, and evaporation: Uniform profile for $K=5.0$, $\beta=0.001$, $\bar{E}=1.0$, $\Theta_R=\Theta_A=2.0$, $m=3$, and $\lambda=\bar{\eta}=0.1$ at $t=0.9994$. Also shown is the inner solution profile, w. In this case, the value of $f(\Theta_{00})<0$ so there is a slight bulge in the droplet profile in the immediate vicinity of the contact line. This is a very small effect and is not directly visible in the corresponding uniform solution shown.

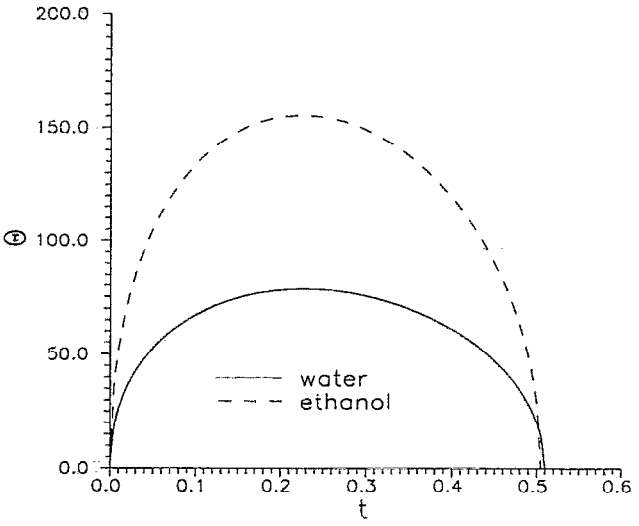

FIG. 19. Large capillary number, unsteady spreading, and evaporation: leading-order solution for $\Theta(t)$ vs t for parameter value estimates for water and ethanol as shown for $\epsilon=0.005$ in Table II. In each case, the value of Θ gets exceedingly large, limiting quantitative conclusions. However, qualitatively these results suggest that for these two systems, the value of the contact angle may be approaching $\pi/2$.

ure 17 shows a single profile for $t=0.9994$ ($s=1.0$) and $\lambda=\bar{\eta}=0.1$. Included on this plot is the inner solution w appearing in Eq. (53). Here we can see the range affected by the inner solution. Note that in this case $f(\Theta_{00})<0$ (see Fig. 16 and note that $\Theta_R=2.0$) so there is a bulge in the immediate vicinity of the contact line. Again this is a very small effect which is not visible when the uniform solution is plotted.

The general behavior for small values of K can be seen in the solutions plotted for water and ethanol in Figs. 18 and 19; the second case listed in Table II, for $\epsilon=0.005$. These figures show leading-order results, which depend only on K. Figure 18 shows a monotonic decrease in the droplet radius, while Fig. 19 shows that the contact angle, Θ gets very large. For small values of K, Θ_{00} becomes large and higher-order corrections shown in Eqs. (47) and (52) also get large. Therefore, λ and $\bar{\eta}/\bar{E}$ must be taken correspondingly small to obtain valid results. Since our model is based on a small-slope theory, quantitative conclusions cannot be made when Θ is large; however, qualitatively these results suggest that the contact angle gets large. This is consistent with the results of Chung and Bankoff,[22] who have found through experimental investigations and analysis from their static rivulet and dry-patch models that large contact angles are seen.

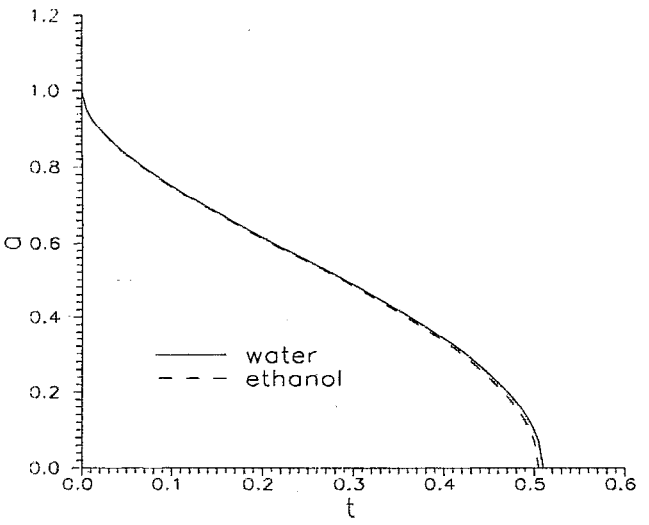

FIG. 18. Large capillary number, unsteady spreading, and evaporation: leading-order solution for $a(t)$ vs t for parameter value estimates for water and ethanol as shown for $\epsilon=0.005$ in Table II. The corresponding contact angle for each case is shown in Fig. 19.

It is interesting to note that since the outer solution satisfies Eq. (34) with the spatial derivatives absent, the initial profile evolves in time only through bulk mass loss. The initial conditions we considered corresponded to parabolic profiles. However, if we were to consider an initial profile with a dimple in the center, for example, we would expect that the drop profile will eventually evolve into two drops, separated by a dryout region. In the case of an axisymmetric droplet with a dimple in the center, this might correspond to a circular droplet with a dryout hole in the center.

VII. SUMMARY

We have considered the evaporation of a two-dimensional liquid droplet on a uniformly heated horizontal surface. In our analysis, we have studied the effects of capillarity, thermocapillarity, vapor recoil, viscous spreading, contact-angle hysteresis, and mass loss on the dynamics of the droplet profile and contact-line region. We have used the one-sided model of evaporation of Burelbach, Bankoff, and Davis,[9] which is modified to include the presence of contact

lines. Our model also extends that of Ehrhard and Davis[7] of nonisothermal spreading to include evaporation.

We have formulated a new contact-line condition (5) based on a mass balance across the evaporating interface. In order to obtain a leading-order description, we have assumed that the relation between the macroscopic contact angle and the fluid velocity at the contact line is approximately given by its nonevaporative form. The lack of direct experimental observations of the fluid velocity at the contact line when evaporation is present does not allow for the use of an empirical relation that includes evaporative effects. However, the results, based on our assumption, have been compared whenever possible with existing information and agree with one's expectations. Further, we have identified features of the competition between spreading and evaporation which can be tested experimentally.

Using a lubrication theory, we obtained evolution equations for the droplet profiles for two cases: with and without a mass source in the base. The presence of a mass source in the base allows for the calculation of steady droplet profiles.

We first examined the steady evaporation case. Here we found that when the contact line is stationary, the contact-line condition determines the steady contact angle, Θ_S, which balances spreading with evaporative mass loss. We found that Θ_S is always larger than the advancing contact angle, Θ_A. This result holds for *any* steady evaporating meniscus and is not dependent on the particular configuration in which the steady meniscus is present.

For unsteady spreading and evaporation (with no mass source in the base) we considered three main limits: zero capillary number, small capillary number, and large capillary number.

For zero capillary number, the evolution equation is satisfied by a parabolic droplet profile. The contact angle and droplet radius are determined by the contact-line condition and a global mass-balance condition. We found that although evaporation always causes the droplet to completely disappear, there are two basic regimes in which the dynamics of the contact line differ. The first of these is a "strong" evaporation regime where the droplet radius decreases monotonically in time. The second is a "weak" evaporation regime where the droplet spreads initially. We were also able to identify the effects of contact-angle hysteresis. In terms of the droplet lifetime, we found that effects which tend to decrease the contact angle and thin the drop promote evaporation while those which tend to increase the contact angle and contract the drop delay evaporation.

We discussed the results for small K (highly volatile droplets) and found multiple time regimes in the dynamics of the contact line. One of the pronounced features here is a rapid readjustment of the contact angle and drop radius from the initial conditions. Following this adjustment, the contact angle remains at a nearly constant value, the plateau, much greater than the advancing contact angle, Θ_A, for most of the droplet life (see Fig. 10). The height of the plateau is given by Θ_S, the constant angle predicted by the steady evaporation problem where viscous spreading balances mass flux at the contact line. The presence of such a plateau during unsteady evaporation is a further feature which could be identified in experiments. After the initial readjustment, the droplet radius decreases relatively slowly to zero with approximately the square-root in time. From this analysis we obtained an estimate for the disappearance time [Eq. (28)]. This estimate shows that the disappearance time increases with increasing contact angle and decreases with increasing evaporation number, $\bar{E}$ (i.e., stronger evaporation).

Next, we considered the results for small but nonzero capillary number. Here we identified the effects of thermocapillarity, vapor recoil, and the unsteady and mass loss terms in the evolution equation. We found that thermocapillarity, which transports mass from hot regions (near the contact line) to colder regions (near the top of the droplet), tends to contract the droplet. As a result the contact angle increases and we find that evaporation is delayed. Vapor recoil, which represents a nonuniform pressure acting down on the liquid–vapor interface and which is stronger near the contact line, also acts to contract the drop and make evaporation less efficient. The inclusion of the unsteady and mass loss terms in the evolution equation has a similar effect of increasing the droplet lifetime. While this may seem counterintuitive, the combined effect of these terms is to transport mass from the contact-line region toward the droplet center, steepening the base. The end result is that evaporation is delayed.

Finally, we have treated the large capillary number limit in the absence of thermocapillarity and vapor recoil. Here we have also taken $\bar{\eta}/\bar{E}$ (the measure of viscous spreading in the contact-line condition) to be small. We found that the droplet profile could be described by an outer region, away from the contact line where the pressure jump due to surface tension can be neglected, and an inner region near the contact line where the effects of curvature and slip are important. We find that the inner region corresponds to a spatially oscillating solution which decays away from the contact line (see Fig. 11). Depending on the sign of $f(\Theta)$, the characteristic of the velocity dependence of the contact angle, these oscillations may correspond to either a dip or bulge of the liquid–vapor interface immediately adjacent to the contact line. We find, however, that these oscillations are typically not observable in plots of the uniform solution (see Figs. 14 and 17). We also find that the droplet radius always decreases monotonically (see Figs. 18, 12, and 15) while the contact angle may get large when K is small but may also decrease monotonically for larger values of K (see Figs. 19, 13, and 16).

It should be noted that a variety of instabilities have been reported under similar circumstances to those we have described here. Contact-line instabilities found under isothermal conditions, as well as thermally induced instabilities and instabilities related to evaporation may be present here. Ehrhard[8] performed experiments for droplet spreading and observed wavy instabilities at the contact line under both isothermal and nonisothermal conditions. Cazabat *et al.*[27] observed a fingering instability of a liquid film rising under Marangoni forces produced by an underlying temperature gradient. They found that the fingers develop from a liquid rim that builds up at the leading edge as a result of the Marangoni flow. Redon *et al.*[28] observed a "festoon" instability during the spreading of a volatile liquid droplet. There

was no external temperature gradient, but evaporation near the contact line increased the local surface tension so that Marangoni flow was induced and a liquid rim formed at the edge of the drop. While the Marangoni flow found in our case is directly opposite from that observed in Cazabat *et al.*[27] and Redon *et al.*,[28] the potential for thermally induced instabilities in our problem should be kept in mind. Finally, instabilities due to evaporative effects such as vapor recoil (e.g., see Palmer,[12] Burelbach, Bankoff, and Davis,[9] and references therein) may play a role here.

ACKNOWLEDGMENTS

The authors would like to thank Dr. D. A. Huntley, Dr. P. G. LaRose, Dr. B. S. Tilley, and Professors M. J. Miksis and J. B. Grotberg for helpful discussions. This work was supported by grants from the National Aeronautics and Space Administration through the Graduate Student Researchers Program (DMA) and the Program on Microgravity Science and Applications (SHD).

APPENDIX A: $O(\bar{C})$ PROFILE CORRECTION

The following is the representation for the $O(\bar{C})$ correction to the droplet profile in the $\bar{C}\ll 1$ analysis of Sec. VI B:

$$h_1(x,\tau)=(\Theta a)_\tau f_1(x;a,\Theta)+\left(\frac{\Theta}{a}\right)_\tau f_2(x;a,\Theta)+f_3(x;a,\Theta)+f_4(x;a,\Theta)+f_5(x;a,\Theta), \tag{A1a}$$

where

$$f_i(x;a,\Theta)=\frac{a^2-x^2}{2a}\int_0^a F_i(\xi;a,\Theta)\,d\xi-\frac{1}{2}\int_0^a (a-\xi)F_i(\xi;a,\Theta)\,d\xi+\frac{1}{2}\int_0^x \frac{(x-\xi)^2}{a-\xi}F_i(\xi;a,\Theta)\,d\xi \tag{A1b}$$

for $i=1,\ldots,5$ with

$$F_1(x;a,\Theta)=\frac{(2a/\Theta)^2}{2(a+x)^2(\beta+\frac{1}{3}h_0)}, \tag{A1c}$$

$$F_2(x;a,\Theta)=-\frac{(2a/\Theta)^2(a^2+ax+x^2)}{6(a+x)^2(\beta+\frac{1}{3}h_0)}, \tag{A1d}$$

$$F_3(x;a,\Theta)=\bar{E}\,\frac{(2a/\Theta)^3}{a^\dagger(a+x)^2(\beta+\frac{1}{3}h_0)}\left(\frac{\tanh^{-1}(a/a^\dagger)-\tanh^{-1}(x/a^\dagger)}{a-x}\right), \tag{A1e}$$

$$F_4(x;a,\Theta)=-\bar{M}K\left(\frac{2a}{\Theta}\right)\frac{h_{0x}(\beta+\frac{1}{2}h_0)}{(a+x)(K+h_0)^2(\beta+\frac{1}{3}h_0)}, \tag{A1f}$$

$$F_5(x;a,\Theta)=-\frac{2\bar{E}^2}{\bar{\rho}}\frac{h_{0x}}{(K+h_0)^3}(a-x), \tag{A1g}$$

and $a^\dagger=[(2aK/\Theta)+a^2]^{1/2}$.

APPENDIX B: OUTER SOLUTION FOR $\bar{C}\gg 1$

The following is the correction, h_1, to the outer solution profile for the large capillary number analysis of Sec. VI C:

$$h_1(x,s)=\frac{1}{P^{1/2}}\left(-t_1(s)+\frac{1}{4}r_1(x)[P^{-2}-P_0^{-2}]+\frac{1}{3}r_2(x)[P^{-3/2}-P_0^{-3/2}]+\frac{1}{2}r_3(x)[P^{-1}-P_0^{-1}]+r_4(x)[P^{-1/2}-P_0^{-1/2}]-\frac{1}{2}r_5(x)[\ln P-\ln P_0]-r_6(x)[P^{1/2}-P_0^{1/2}]-\frac{1}{2}r_7(x)[P-P_0]-\frac{1}{3}r_8(x)[P^{3/2}-P_0^{3/2}]-\frac{1}{4}r_9(x)[P^2-P_0^2]-\frac{1}{5}r_{10}(x)[P^{5/2}-P_0^{5/2}]\right), \tag{B1}$$

where $P=[h_0(x,s)+K]^2$ and $P_0=[h_0(x,0)+K]^2$. The coefficients, $r_i(x)$, are functions only of x and are listed below.

The function $t_1(s)$ is given by

$$t_1(s)=\tfrac{1}{4}r_1(a_0)[P_a^{-2}-P_{0a}^{-2}]+\tfrac{1}{3}r_2(a_0)[P_a^{-3/2}-P_{0a}^{-3/2}]+\tfrac{1}{2}r_3(a_0)[P_a^{-1}-P_{0a}^{-1}]+r_4(a_0)[P_a^{-1/2}-P_{0a}^{-1/2}]-\tfrac{1}{2}r_5(a_0)[\ln P_a-\ln P_{0a}]-r_6(a_0)[P_a^{1/2}-P_{0a}^{1/2}]-\tfrac{1}{2}r_7(a_0)[P_a-P_{0a}]-\tfrac{1}{3}r_8(a_0)[P_a^{3/2}-P_{0a}^{3/2}]-\tfrac{1}{4}r_9(a_0)[P_a^2-P_{0a}^2]-\tfrac{1}{5}r_{10}(a_0)[P_a^{5/2}-P_{0a}^{5/2}], \tag{B2}$$

where $P_a=K^2$, $P_{0a}=K^2+2s$, and $r_i(a_0)$ are shown below.

The following are the coefficients which appear in the $O(\lambda)$ correction to the outer solution equation (B1) and the strained time coordinate in Eq. (B2) for the large capillary number analysis of Sec. VI C:

$$r_1(x)=\tfrac{15}{16}K^2(\beta-\tfrac{1}{3}K)(c_1')^4, \tag{B3a}$$

$$r_2(x)=\tfrac{3}{4}K(K-2\beta)(c_1')^4, \tag{B3b}$$

$$r_3(x)=\tfrac{9}{16}(\beta-K)(c_1')^4-\tfrac{9}{4}K^2(\beta-\tfrac{1}{3}K)(c_1')^2c_1'', \tag{B3c}$$

$$r_4(x)=\tfrac{1}{8}(c_1')^4-\tfrac{15}{8}K(K-2\beta)(c_1')^2c_1'', \tag{B3d}$$

$$r_5(x)=\tfrac{3}{2}(K-\beta)(c_1')^2c_1''+K^2(\beta-\tfrac{1}{3}K)[\tfrac{3}{4}(c_1'')^2+c_1'c_1'''], \tag{B3e}$$

$$r_6(x)=\tfrac{3}{4}K(K-2\beta)c_1'c_1'''-\tfrac{3}{8}(c_1')^2c_1''+\tfrac{3}{4}K(K-2\beta)\times(c_1'')^2, \tag{B3f}$$

$$r_7(x)=(\beta-K)[\tfrac{3}{4}(c_1'')^2+\tfrac{1}{2}c_1'c_1''']-\tfrac{1}{2}K^2(\beta-\tfrac{1}{3}K)c_1'''', \tag{B3g}$$

$$r_8(x)=\tfrac{1}{12}c_1'c_1'''+\tfrac{1}{4}(c_1'')^2-\tfrac{1}{2}K(K-2\beta)c_1'''', \tag{B3h}$$

$$r_9(x)=-\tfrac{1}{2}(\beta-K)c_1'''', \tag{B3i}$$

$$r_{10}(x)=-\tfrac{1}{6}c_1'''', \tag{B3j}$$

where

$$c_1'=-4x(1-x^2+K). \tag{B4}$$

[1]F. J. Renk and P. C. Wayner, Jr., "An evaporating ethanol meniscus, Part I: Experimental studies," ASME J. Heat Trans. **101**, 55 (1979).

[2]F. J. Renk and P. C. Wayner, Jr., "An evaporating ethanol meniscus, Part II: Analytical studies," ASME J. Heat Trans. **101**, 59 (1979).

[3]S. Moosman and G. M. Homsy, "Evaporating menisci of wetting fluids," J. Colloid Interface Sci. **73**, 212 (1980).

[4]M. Sujanani and P. C. Wayner, Jr., "Transport processes and interfacial phenomena in an evaporating meniscus," Chem. Eng. Comm. **118**, 89 (1992).

[5]D. Ripple, "Dynamic contact angle of a liquid spreading on a heated plate" (preprint, 1994).

[6]P. C. Wayner, Jr., "Spreading of a liquid film with a finite contact angle by the evaporation/condensation process," Langmuir **9**, 294 (1993).

[7]P. Ehrhard and S. H. Davis, "Non-isothermal spreading of liquid drops on horizontal plates," J. Fluid Mech. **229**, 365 (1991).

[8]P. Ehrhard, "Experiments on isothermal and non-isothermal spreading," J. Fluid Mech. **257**, 463 (1993).

[9]J. P. Burelbach, S. G. Bankoff, and S. H. Davis, "Nonlinear stability of evaporating/condensing liquid films," J. Fluid Mech. **195**, 463 (1988).

[10]E. B. Dussan V., "On the spreading of liquids on solid surfaces: static and dynamic contact lines," Annu. Rev. Fluid. Mech. **11**, 371 (1979).

[11]S. H. Davis, "Contact-line problems in fluid mechanics," J. Appl. Mech. **50**, 977 (1983).

[12]H. J. Palmer, "The hydrodynamic stability of rapidly evaporating liquids at reduced pressure," J. Fluid Mech. **75**, 487 (1976).

[13]P. C. Wayner, Jr., "The effect of interfacial mass transport on flow in thin liquid films," Colloids Surfaces **52**, 71 (1991).

[14]V. P. Carey, *Liquid–Vapor Phase-Change Phenomena: An Introduction to the Thermophysics of Vaporization and Condensation Processes in Heat Transfer Equipment* (Hemisphere, Washington, DC, 1992), pp. 112–120.

[15]A. M. Schwartz and S. B. Tejada, "Studies of dynamic contact angles on solids," J. Colloid Interface Sci. **38**, 359 (1972).

[16]R. L. Hoffman, "A study of the advancing interface. I. Interface shape in liquid–gas systems," J. Colloid Interface Sci. **50**, 228 (1975).

[17]H. P. Greenspan, "On the motion of a small viscous droplet that wets a surface," J. Fluid Mech. **84**, 125 (1978).

[18]L. M. Hocking, "The spreading of thin drops by gravity and capillarity," Q. J. Mech. Appl. Math. **36**, 55 (1983).

[19]P. J. Haley and M. J. Miksis, "The effects of the contact line on droplet spreading," J. Fluid Mech. **223**, 57 (1991).

[20]D. M. Anderson, "Corner flows, heat transfer, and phase transformation," Ph.D. thesis, Northwestern University, Evanston, IL, 1993.

[21]L. M. Hocking, "Sliding and spreading of thin two-dimensional drops," Q. J. Mech. Appl. Math. **34**, 37 (1981).

[22]J. C. Chung and S. G. Bankoff, "Initial breakdown of a heated liquid film in cocurrent two-component annular flow. 2. Rivulet and drypatch models," Chem. Eng. Comm. **4**, 455 (1980).

[23]S. Rosenblat and S. H. Davis, "How do liquid drops spread on solids?," in *Frontiers in Fluid Mechanics*, edited by S. H. Davis and J. L. Lumley (Springer-Verlag, Berlin, 1985).

[24]M. Van Dyke, *Perturbation Methods in Fluid Mechanics* (Academic, New York, 1964).

[25]J. B. Keller and M. J. Miksis, "Surface tension driven flows," SIAM J. Appl. Math. **43**, 268 (1983).

[26]J. B. Lawrie, "Surface-tension-driven flow in a wedge," Q. J. Mech. Appl. Math. **43**, 251 (1990).

[27]A. M. Cazabat, F. Heslot, S. M. Troian, and P. Carles, "Fingering instability of thin spreading films driven by temperature gradients," Nature **346**, 824 (1990).

[28]C. Redon, F. Brochard-Wyart, and F. Rondelez, "Festoon instabilities of slightly volatile liquids during spreading," J. Phys. II(France) **2**, 1671 (1992).